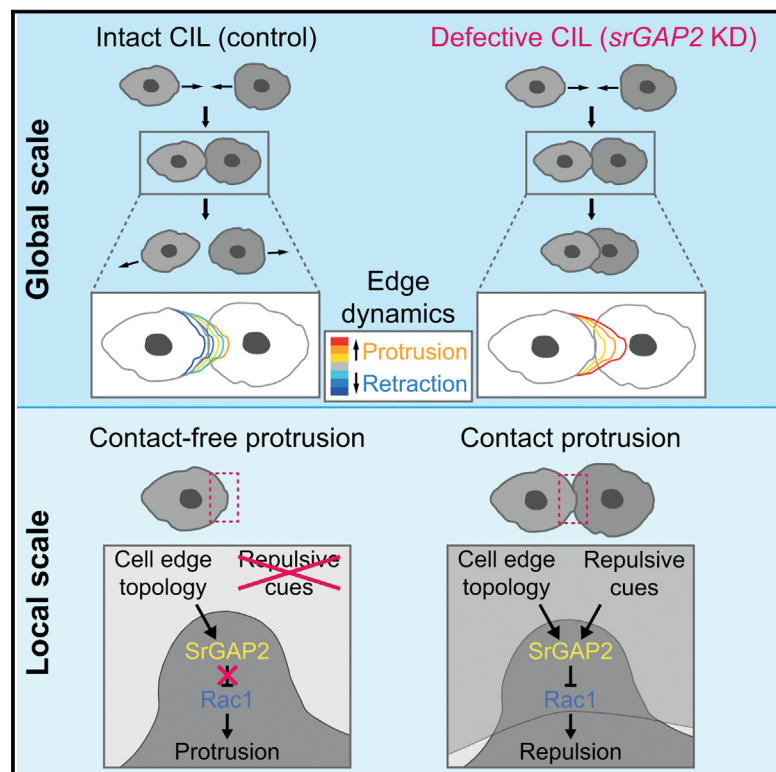


Developmental Cell

SrGAP2-Dependent Integration of Membrane Geometry and Slit-Robo-Repulsive Cues Regulates Fibroblast Contact Inhibition of Locomotion

Graphical Abstract



Authors

Rafael Dominik Fritz, Denis Menshykau, Katrin Martin, Andreas Reimann, Valeria Pontelli, Olivier Pertz

Correspondence

olivier.pertz@izb.unibe.ch

In Brief

Fritz et al. show that Rac GAP srGAP2 and Slit-Robo signaling regulate contact inhibition of locomotion in fibroblasts. srGAP2 regulates dynamics of contact protrusions that stochastically explore cell-cell overlaps and integrates edge curvature and Slit-Robo-mediated repulsive cues to locally cease Rac1 activity for cell repulsion, repolarization, and migrational direction change.

Highlights

- SrGAP2 is required for cell repulsion and contact inhibition of locomotion (CIL)
- Local fine-tuning of edge dynamics at cell-cell overlaps determines cell repulsion
- SrGAP2 integrates geometrical and Slit-Robo-repulsive cues to elicit CIL
- SrGAP2 controls Rac1 activity duration in contact, but not contact-free, protrusions

SrGAP2-Dependent Integration of Membrane Geometry and Slit-Robo-Repulsive Cues Regulates Fibroblast Contact Inhibition of Locomotion

Rafael Dominik Fritz,¹ Denis Menshykau,^{2,4} Katrien Martin,¹ Andreas Reimann,^{1,5} Valeria Pontelli,³ and Olivier Pertz^{1,6,*}

¹Department of Biomedicine, University of Basel, Mattenstrasse 28, 4058 Basel, Switzerland

²Department of Biosystems, Science and Engineering (D-BSSE), ETH Zurich, Mattenstrasse 26, 4058 Basel, Switzerland

³Department of Neurological and Movement Sciences, Section of Physiology, University of Verona, Strada le Grazie 8, 37134 Verona, Italy

⁴Present address: Bayer Technology Services GmbH, Computational Systems Biology, 51368 Leverkusen, Germany

⁵Present address: Department of Biosystems, Science and Engineering (D-BSSE), ETH Zurich, Mattenstrasse 26, 4058 Basel, Switzerland

⁶Present address: Institute of Cell Biology, University of Bern, Baltzerstrasse 4, 3012 Bern, Switzerland

*Correspondence: olivier.pertz@izb.unibe.ch

<http://dx.doi.org/10.1016/j.devcel.2015.09.002>

SUMMARY

Migrating fibroblasts undergo contact inhibition of locomotion (CIL), a process that was discovered five decades ago and still is not fully understood at the molecular level. We identify the Slit2-Robo4-srGAP2 signaling network as a key regulator of CIL in fibroblasts. CIL involves highly dynamic contact protrusions with a specialized actin cytoskeleton that stochastically explore cell-cell overlaps between colliding fibroblasts. A membrane curvature-sensing F-BAR domain pre-localizes srGAP2 to protruding edges and terminates their extension phase in response to cell collision. A FRET-based biosensor reveals that Rac1 activity is focused in a band at the tip of contact protrusions, in contrast to the broad activation gradient in contact-free protrusions. SrGAP2 specifically controls the duration of Rac1 activity in contact protrusions, but not in contact-free protrusions. We propose that srGAP2 integrates cell edge curvature and Slit-Robo-mediated repulsive cues to fine-tune Rac1 activation dynamics in contact protrusions to spatiotemporally coordinate CIL.

INTRODUCTION

Contact inhibition of locomotion (CIL) was first described more than 50 years ago by Abercrombie as a general cell repulsion phenomenon between two contacting fibroblasts (Abercrombie and Heaysman, 1953, 1954). Nowadays, CIL is considered a generic mechanism to locally cease cell protrusions in vitro and in vivo (Mayor and Carmona-Fontaine, 2010). CIL consists of two phases: initial cell-cell contact and collapse of protrusions followed by cell repolarization and change of migrational direction (Mayor and Carmona-Fontaine, 2010). Cadherins (Scarpa et al., 2015; Theveneau et al., 2010; Huttenlocher et al., 1998), nectins (Takai et al., 2008), heparan sulfate

proteoglycans (HSPGs) (Matthews et al., 2008), Ephrins (Astin et al., 2010; Sugiyama et al., 2013), and non-canonical Wnt signaling (Carmona-Fontaine et al., 2008) have been shown to regulate CIL. In many cases, this feeds into the control of cytoskeletal dynamics through Rho GTPases (Carmona-Fontaine et al., 2008; Matthews et al., 2008; Theveneau et al., 2010; Scarpa et al., 2015). However, the precise molecular link between such cell surface molecules and small GTPases remains elusive.

Rho GTPases are key regulators of the cytoskeletal dynamics that control cell migration (Burridge and Wennerberg, 2004; Heasman and Ridley, 2008; Machacek et al., 2009; Pertz et al., 2006; Ridley, 2006). Their activity is tightly controlled in time and space by guanine nucleotide exchange factors (GEFs) and GTPase-activating proteins (GAPs) that respectively activate and inhibit GTPases. Regulation of Rho GTPases by different GEFs and GAPs, as well as coupling to specific downstream effectors, dictates the overall outcome of Rho GTPase signaling at any given subcellular localization (Pertz, 2010). Recent studies, in which spatiotemporal Rho GTPase activation dynamics have been measured using fluorescence resonance energy transfer (FRET)-based biosensors, have revealed complex spatiotemporal signaling programs in which the activity of multiple Rho GTPases fluctuates on time and length scales of tens of seconds and single micrometers (Kraynov et al., 2000; Machacek et al., 2009; Nalbant et al., 2004; Pertz et al., 2006). An important question is, therefore, how global properties such as cell migration speed and persistence emerge from such exquisite spatiotemporal control of Rho GTPases at smaller lengths and timescales.

Slit-Robo GAP (srGAP) proteins transduce repulsive cues downstream of the Slit-Robo axon guidance pathway to inhibit Rho GTPases (Wong et al., 2001; Ypsilanti et al., 2010). SrGAP2 regulates cell migration and neurite outgrowth in neuronal cells as well as brain development (Charrier et al., 2012; Dennis et al., 2012; Guerrier et al., 2009; Pertz et al., 2008).

Here we report that the Slit-Robo pathway controls fibroblast CIL. We find that srGAP2 specifically regulates the dynamics of specialized contact protrusions that stochastically explore cell-cell overlaps at minute timescales. SrGAP2 regulates a specific spatiotemporal pool of Rac1 activity within contact protrusions,

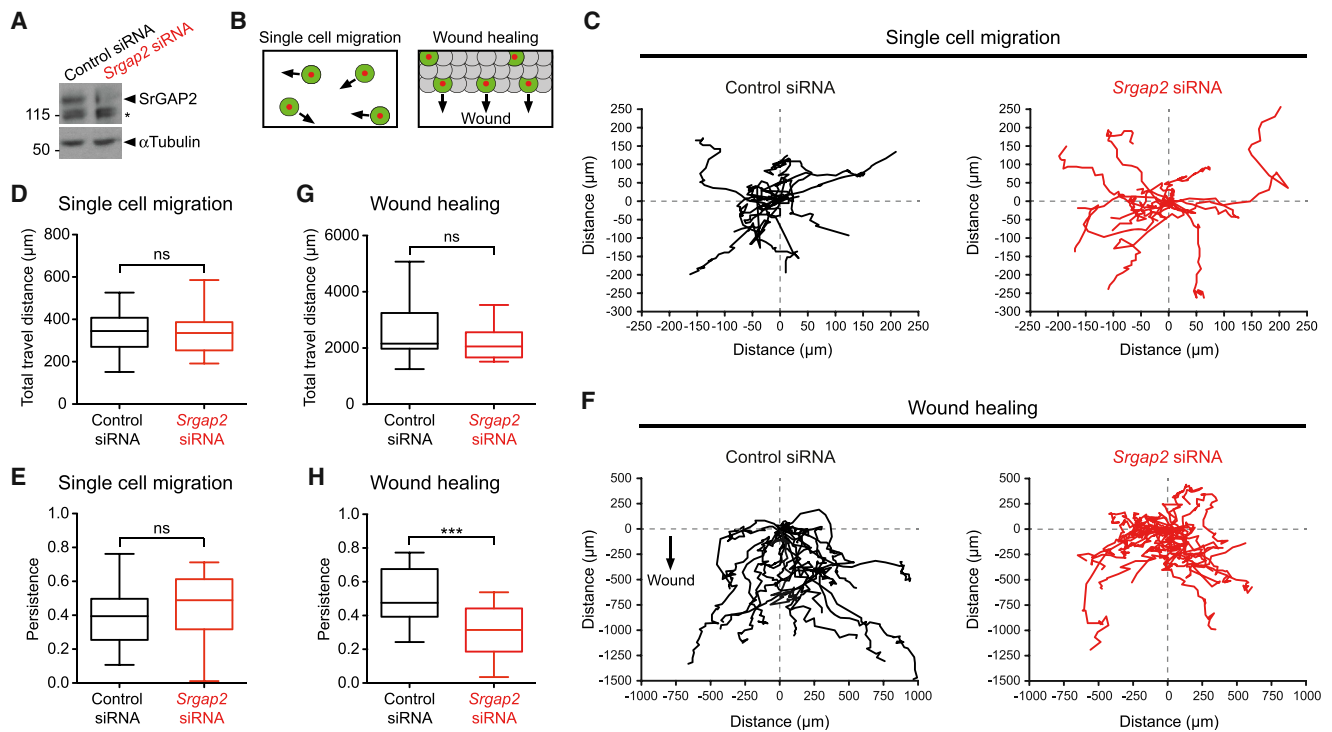


Figure 1. SrGAP2 Regulates the Directional Persistence of Cells Migrating in Sheets, but Not in Isolation

(A) Western blot analysis of *Srgap2* KD efficiency. Cells were transfected with non-targeting siRNA (control) or with a pool of four *Srgap2* siRNAs. Asterisk points to an unspecific band. Numbers depict molecular weight in kilodaltons.

(B) Cell migration assays schematics. Fibroblasts stably expressing Lifeact-GFP/nuclear localization sequence (NLS)-mCherry (green cell with red nuclei), transfected with control or *Srgap2* siRNA, were seeded either sparsely or within a monolayer of untransfected WT cells (gray). NLS-mCherry signal was used to track cells.

(C) Migration tracks of sparsely seeded control or *Srgap2* KD cells are shown (n = 14 cells for each condition).

(D and E) Quantification gives total travel distance (D) and directional persistence (E) of cells shown in (C).

(F) Migration tracks of control (n = 19) and *Srgap2* KD cells (n = 22) embedded in a wounded monolayer. Arrow indicates the direction into the wound.

(G and H) Quantification gives total travel distance (G) and directional persistence (H) of cells shown in (F).

Boxplots show median, interquartile range (IQR) (box), and 1.5 IQR (whiskers) (D, E, G, and H). Two-tailed unpaired Student's t test; ***p < 0.001; ns, not significant.

but is dispensable for contact-free protrusions. At the whole-cell scale, this stochastic process fine-tunes protrusion collapse and cell repolarization to mediate CIL.

RESULTS

SrGAP2 Regulates Contact-Dependent Cell Migration

Using proteomics, we discovered srGAP2 to be expressed in NIH 3T3 mouse fibroblasts (Fengos et al., 2014). Given the importance of srGAP2 in neuronal cell migration (Guerrier et al., 2009) and growth cone dynamics (Pertz et al., 2008), we hypothesized that srGAP2 also regulates fibroblast motility. We therefore downregulated *Srgap2* by RNAi and tracked subconfluent randomly migrating cells (Figures 1A and 1B). Surprisingly, *Srgap2* knockdown (KD) neither affected total travel distance nor persistence of migration (Figures 1C–E). Next we analyzed *Srgap2* KD cells in a wound-healing assay, where migration is influenced by contacts with neighboring cells (Figure 1B). Despite identical total travel distances, *Srgap2* KD cells did not persistently migrate into the wound as was observed for control cells (Figures 1F–H). Thus, srGAP2 regulates cell contact-

dependent, directional persistence of migration in monolayers, but not cell migration per se.

SrGAP2 Regulates CIL and Restricts Cell-Cell Overlap through Repulsion

Because srGAP proteins mediate cell repulsion in neuronal cells (Wong et al., 2001), the loss of contact-dependent directional persistence might be attributed to defects in this process. We therefore examined the behavior of sparsely seeded fibroblasts during cell-cell collision. Control cells underwent proper CIL characterized by cell repulsion and reversal of migrational direction upon cell-cell collision. In contrast, cells treated with *Srgap2* small interfering RNA (siRNA) or small hairpin RNA (shRNA) were CIL deficient, because they neither repulsed each other nor reversed the direction of migration after collision (Figures 2A–2C; Movie S1). Quantification of the cell-cell collision-dependent change of migrational direction revealed that control cells migrate in the opposite direction, while *Srgap2* KD cells continue to migrate with little deviation from their original direction (Figures 2D and 2E). Additionally, *Srgap2* KD cells remained in contact for longer time periods compared to control cells, further

indicating that srGAP2 controls cell-cell repulsion (Figure 2F). We obtained similar results in primary mouse embryonic fibroblasts (MEFs) (Figures S1A–S1D).

We then produced fibroblasts stably expressing Lifeact-GFP or Lifeact-mCherry, which visualizes F-actin dynamics (Riedl et al., 2008) and properly outlines the cell border (Figures S2A–S2C). This allowed us to unambiguously evaluate cell-cell overlap in differentially labeled, adjacent cells. Unexpectedly, we found control cells to markedly overlap. This cell-cell overlap, however, increased in *Srgap2* KD cells (Figure 2G; Movie S2). Moreover, cell-cell overlap was stable in time in control cells, but rose constantly in *Srgap2* KD cells (Figure 2H). Cell size itself did not impact on cell-cell overlap given the weak correlation between both parameters (Figure 2I). *Srgap2* KD, Lifeact-GFP cells embedded in confluent Lifeact-mCherry monolayers revealed increased cell-cell overlap compared to control Lifeact-GFP cells (Figures 2J and 2K). Identical results were observed in the converse experiment. Furthermore, *Srgap2* KD in both the monolayer and the embedded cells led to a further increase in cell-cell overlap, indicating that both interacting cells determine the degree of cell-cell overlap. Importantly, we found that *Srgap2* KD did not affect spreading in subconfluent fibroblast (Figure 2L), indicating that srGAP2 only functions in the context of overlapping cells. This also was observed in primary MEFs (Figure S1E). In summary, srGAP2 regulates cell repulsion by maintaining the size of cell-cell overlap regions constant, both in sparsely seeded contacting cells and in confluent monolayers of immortalized and primary mouse fibroblasts.

Cell-Cell Overlap Zones Are Constantly Explored by Dynamic Contact Protrusions

We then explored which mechanism regulates the maintenance of steady-state cell-cell overlap. This implies the formation of protrusions crawling either below or on top of neighboring cells (Figure 3A). To discriminate between both possibilities, we imaged adjacent Lifeact-GFP and Lifeact-mCherry cells. We found the following: (1) cell-cell overlaps consisted of multiple contact protrusions characterized by highly dynamic lamellipodia and filopodia, as compared to contact-free edges (Figure 3B; Movie S3); (2) total internal reflection fluorescence (TIRF) imaging revealed that these contact protrusions remain associated with the extracellular matrix while infiltrating below neighboring cell edges, which become displaced from the TIRF field (Figure 3C); this is a stereotypic behavior observed in 100% of cases analyzed (>100 protrusions); and (3) contact, but not contact-free, protrusions displayed an intense F-actin band directly at their tip that assembled as soon as contact protrusions extended beneath adjacent cells and disassembled instantly during edge retraction (Figures 3D–3F; Figures S1F and S1G; Movie S4).

Kymograph-based quantification of edge dynamics revealed that contact protrusions were more dynamic than contact-free protrusions (Figure 3G), due to not only enhanced membrane protrusion (Figure 3H) but also retraction (Figure 3I). Despite such enhanced edge motility in contact protrusions, there was no effect on net edge movement (Figure 3J). Colliding cells undergo repolarization during CIL and establish new contact-free protrusions away from the site of cell-cell

contact. We compared contact-free protrusions in isolated cells and in cells engaged in cell-cell overlap and found that contact-free protrusions in the latter were more dynamic and persistent than in isolated cells (Figures S2D–S2G). Together, these results show that maintenance of steady-state cell-cell overlap is mediated by highly dynamic, extending and retracting contact protrusions with a specialized F-actin cytoskeleton.

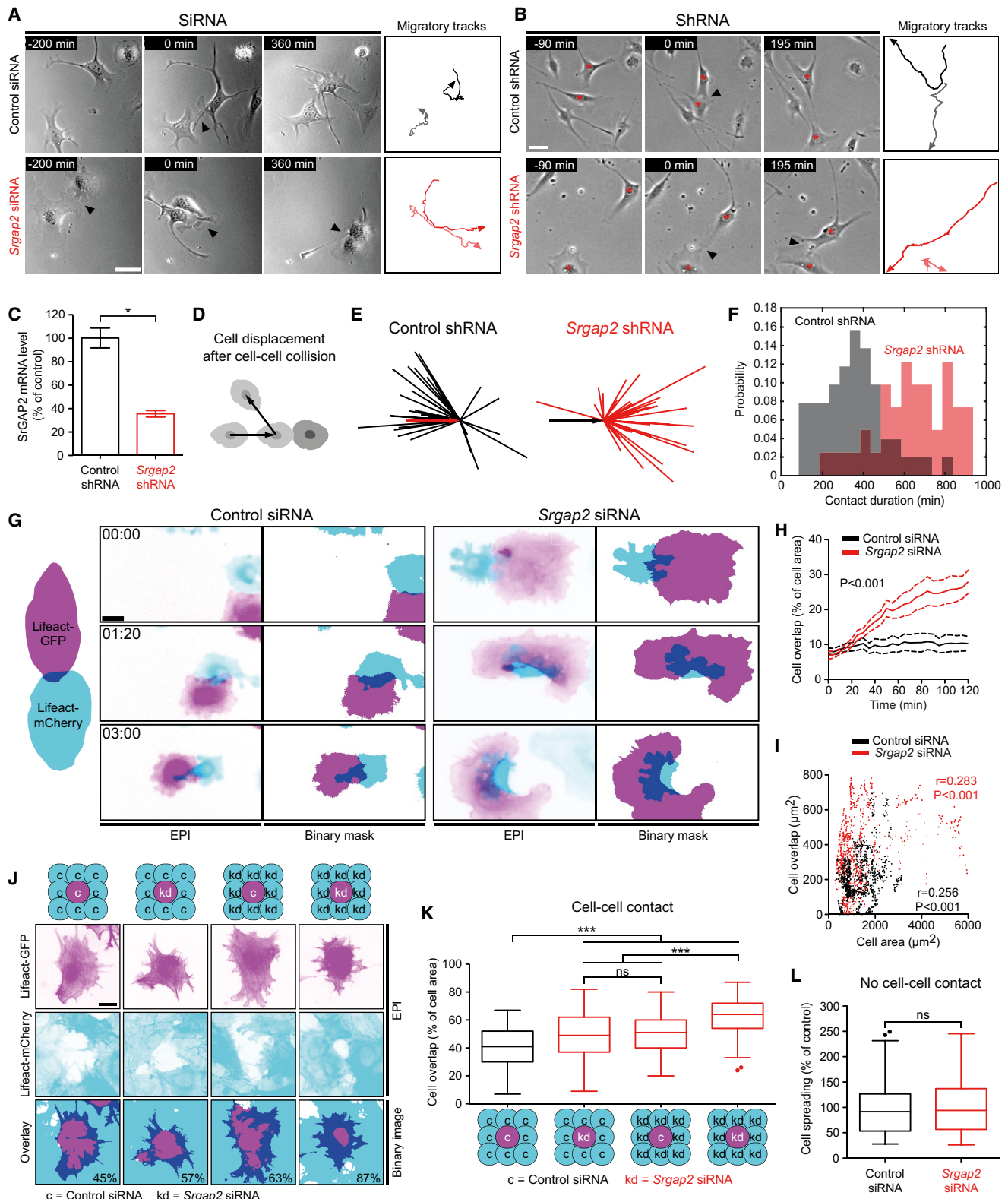
SrGAP2 Specifically Regulates the Extension Phase of Contact Protrusions

Since maintenance of cell-cell overlap is a highly dynamic process, we explored if srGAP2 regulates contact protrusion dynamics. Consistent with the findings that srGAP2 does not regulate intrinsic cell migration nor spreading (Figures 1 and 2), we observed that contact-free edge dynamics were not affected by *Srgap2* KD (Figures 3K–3O, first and second columns from left). In contrast, *Srgap2* KD increased total and net edge movement as well as persistence of contact protrusions (Figures 3K–3M). This arose from increased edge protrusion (Figure 3N), while edge retraction was only minimally affected (Figure 3O). Protrusion and retraction frequencies also were not affected (Figures S2H and S2I). Thus, *Srgap2* KD enhances the extension of contact, but not contact-free, protrusions (schematized in Figure 3P), indicating that srGAP2 specifically limits the extension phase of contact protrusions.

Endogenous srGAP2 Localizes to Protrusions with Curved Edges

We then evaluated the subcellular localization of srGAP2 in subconfluent, polarized cells. Epifluorescence imaging indicated leading edge but also perinuclear srGAP2 localization. TIRF imaging, however, revealed that srGAP2 specifically localizes to the ventral part of contact-free protrusions, with some accumulation at curved cell edges (Figure 4A). SrGAP2 contains a Fes/CIP4 homology-Bin/Amphiphysin/Rversus (F-BAR) domain, which has been shown to modulate but also might sense membrane curvature (Frost et al., 2008, 2009; Guerrier et al., 2009). Therefore, we developed an image analysis pipeline to test if srGAP2 localizes to lamellipodial edges in a curvature-dependent manner (Figure S3A).

This pipeline was validated using synthetic image datasets (Figures S3B–S3E). By co-labeling of endogenous srGAP2 and membrane-tethered GFP-CAAX or the transmembrane receptor Robo4, we ensured that the analyzed srGAP2 signal genuinely represented the cell edge (Figures S3F–S3K). In srGAP2-immunostained, contact-free protrusions, we detected more srGAP2 at curved cell edges (Figure 4B, left). To quantify the relationship between curvature and cell edge srGAP2 recruitment, we extracted srGAP2 fluorescence intensity and curvature profiles along the cell border (Figures 4B and 4C), and we observed a positive correlation between both variables (Figure 4D). As a control, analysis of a homogeneously distributed fluorescent signal from exogenously expressed GFP-CAAX did not lead to any correlation (Figures 4E–4G). Analysis of multiple protrusions revealed a distribution shift toward higher correlation coefficients in cells stained for srGAP2 compared to GFP-CAAX (Figure 4H). These data show a correlation between lamellipodial srGAP2 recruitment and edge curvature.

**Figure 2. SrGAP2 Regulates CIL and Maintenance of Cell-Cell Overlap**

(A and B) Phase-contrast time series of control and *Srgap2* KD cells treated with siRNA (A) and shRNA (B) during cell collision. Migration trajectories are summarized to the right. Black arrowheads designate contacts between cell edges.

(C) The qPCR analysis of *Srgap2* KD efficiency is shown. Mean \pm SD; n = 4 measurements; Mann-Whitney test.

(legend continued on next page)

SrGAP2 Dynamically Associates to the Tip of Extending, but Not Retracting, Contact Protrusions

Next, we studied srGAP2 dynamics in contact-free and contact protrusions. As for its endogenously expressed counterpart, exogenous srGAP2-GFP localized to the leading edge of single migrating cells (Figure S4A). Examination of interacting cells revealed that srGAP2-GFP formed a broad gradient in contact-free protrusions (Figures 4I and 4J; Figure S4B; Movie S5), while it localized at a focused band directly at the tip of contact protrusions (Figures 4I and 4K). The latter pattern was reminiscent of the focused F-actin signal previously observed at that location (Figures 3C–3E). SrGAP2-GFP enriched at the edge of growing protrusions in a curvature-dependent manner and dissociated from the cell edge during protrusion collapse (Figure 4L; Figures S4C–S4E). Enrichment of srGAP2-GFP in both contact-free and contact protrusions required the presence of the F-BAR domain, because deletion mutants localized to the cytosol like GFP. In contrast, mutation of the Src homology 3 (SH3) domain (W765A mutant), responsible for interaction with Robo (Guerrier et al., 2009; Li et al., 2006; Wong et al., 2001), did not interfere with membrane targeting (Figure 4M; Figure S4F). Thus, srGAP2 dynamically associates with the cell edge at the tip of extending contact protrusions in an F-BAR-dependent manner, but dissociates during membrane retraction.

The Slit-Robo Pathway Regulates Maintenance of Cell-Cell Overlap and CIL

In neuronal cells, srGAP proteins mediate cell-cell repulsion downstream of Slit and Robo (Wong et al., 2001; Ypsilanti et al., 2010). To explore whether Slit and Robo regulate repulsion in fibroblasts, we designed a robust assay to evaluate cell contact-dependent spreading in response to siRNA perturbations (Figures 5A–5D). Specifically, we evaluated if cells deficient in the repulsion machinery would spread more efficiently due to impaired sensing of repulsive cues received from the monolayer. Using this assay, we confirmed that *Srgap2* KD cells displayed higher spreading than control cells in wild-type (WT) cell monolayers and vice versa, this effect being further increased in *Srgap2* KD monolayers (Figure 5E). This showed again that srGAP2 solely regulates cell spreading influenced by cell-cell interactions.

Next we identified mediators of cell-cell repulsion at each level of the Slit-Robo signaling pathway using siRNA pools. *Srgap1*,

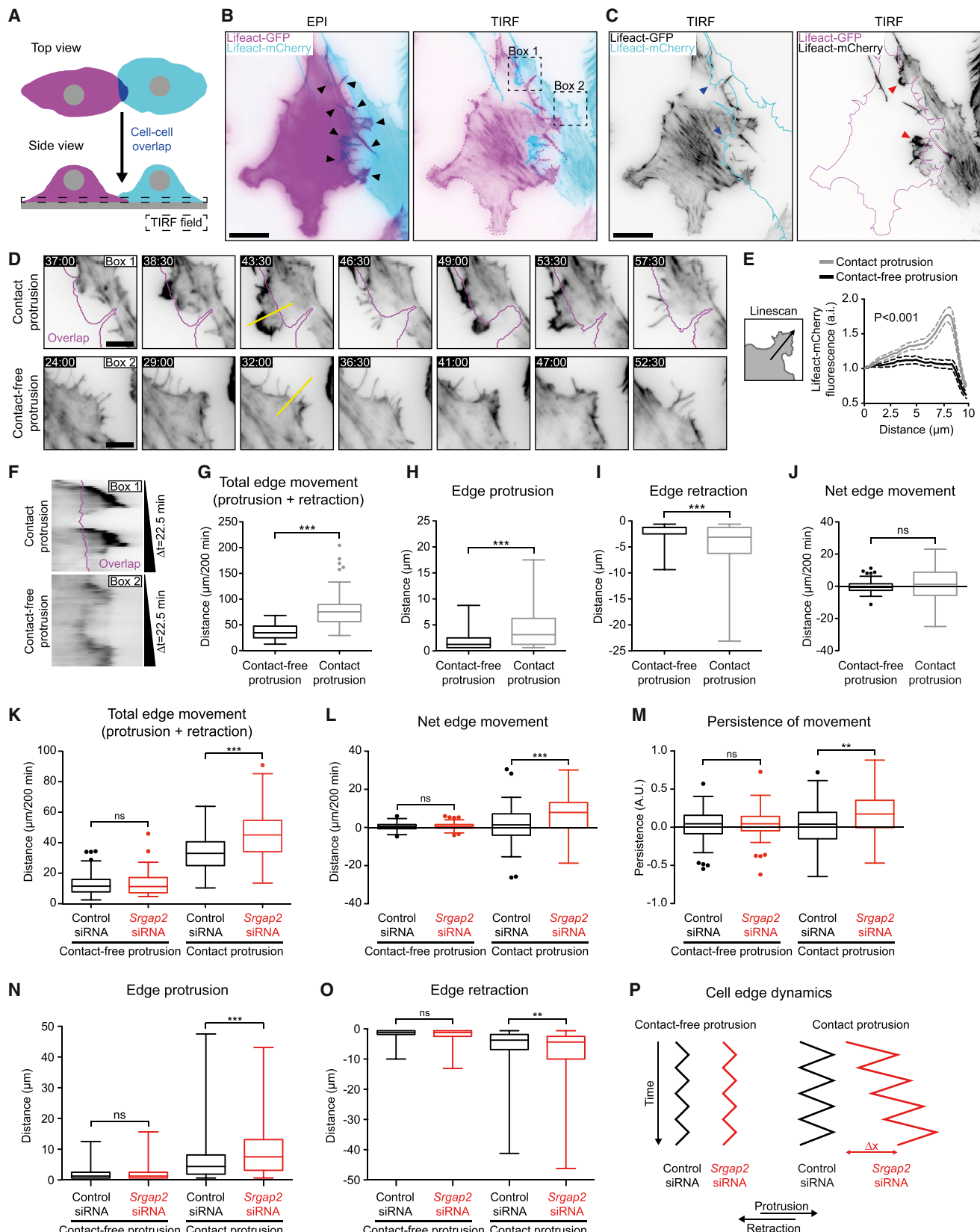
Robo3, *Robo4*, *Slit2*, and *Slit3* KD fostered contact-dependent cell spreading and phenocopied *Srgap2* KD (Figures 5F and 5G). We excluded off-target effects by repeating the assay with single siRNAs for selected genes (Figure 5H). We also confirmed that *Robo4* and *Slit2* KD increased cell-cell overlap in cell monolayers (Figures 5I and 5J). We then examined the subcellular localization of Slit2 and Robo4 by immunofluorescence in subconfluent, polarized cells. Both Slit2 and Robo4 localized mainly to perinuclear endomembranes, most likely corresponding to secretory compartments necessary for secretion. TIRF microscopy, however, revealed broad accumulation of Slit2 at the leading edge, while Robo4 was evenly localized at the plasma membrane with additional enrichment directly at the leading edge (Figure 5K).

Finally, we investigated the impact of Slit2 and Robo4 on CIL in both NIH 3T3 cells and primary MEFs. As observed for *Srgap2* KD, *Slit2* and *Robo4* KD cells were deficient in CIL, because they failed to change the direction of migration after cell-cell collision and displayed prolonged contact duration (Figures 5L–5N; Figures S1H–S1K). These results indicate that the receptor-based repulsion machinery is pre-polarized in contact-free protrusions prior to any cell-cell encounter and activated during CIL.

Construction of a Rac1 FRET Biosensor

To analyze the spatiotemporal regulation of Rac1 by srGAP2, we constructed an improved, second-generation Rac1 FRET biosensor, which we term Rac1-2G. We used our previously described cpFRET toolkit (Fritz et al., 2013), and we took advantage of the GTP-Rac1-sensing domain from the effector PAK1 (Lamarche et al., 1996). The cpFRET toolkit is a biosensor library in which geometric diversity has been built into the fluorophores. This library is screened to empirically identify a biosensor with robust spectral properties. We used a biosensor design that previously successfully yielded an improved RhoA biosensor and at the same time retained interaction with RhoGDI, which is essential to capture faithful spatiotemporal patterns of Rho GTPase activity (Fritz et al., 2013). We identified a biosensor that displayed a robust change in emission ratio (ER) (Figures 6A and 6B; Figures S5A–S5C and S6) and appropriately responded to mutations that affect nucleotide loading (T17N) or the ability of Rac1 to interact with the PAK effector domain (Y40C) (Lamarche et al., 1996; Figure 6C). The biosensor also adequately responded to coexpression of RhoGDI and Rac1-specific GEFs

- (D) Schematic representation shows migrational direction (black arrows) before and after cell-cell collision.
- (E) Scaled cell-displacement vectors of colliding cells. Arrows represent the scaled displacement of all cells before collision, whereas lines show migrational direction of each cell after collision. The length of lines is normalized to the respective arrow ($n = 30$ control and 38 *Srgap2* KD cells).
- (F) Distribution of cell-cell contact duration in control and *Srgap2* KD cells is shown ($n = 50$ and 43 collisions of control and *Srgap2* KD cells, respectively).
- (G) Time series of colliding Lifeact-GFP (magenta) and Lifeact-mCherry (cyan) cells transfected with the indicated siRNAs. Epifluorescence (EPI) channels and their thresholded binary masks are shown in cyan/magenta colors. Timescale, hours:minutes.
- (H) Quantification of cell-cell overlap in time between colliding cells. Cell-cell overlap is normalized to cell area (overlapping area/whole cell area). Graphs represent mean \pm SEM; $n = 16$ control and 14 *Srgap2* KD cells, respectively; Mann-Whitney test.
- (I) Correlation of cell-cell overlap and cell area ($n = 951$ and 1,084 measurements for control and *Srgap2* KD cells, respectively). Spearman correlation coefficient and t statistics are shown.
- (J) Representative images of Lifeact-GFP cells embedded in Lifeact-mCherry monolayers. EPI and composite binary images are shown in cyan/magenta colors. SiRNA treatment is schematized (top). Cell-cell overlap, quantified as percentage of cell size, is displayed (bottom).
- (K) Quantification of normalized cell-cell overlap in monolayers. Boxplots show median, IQR (box), 1.5 IQR (whiskers), and outliers (dots) ($n = 219$, 128, 115, and 112 cells; Bonferroni multiple comparison test).
- (L) Quantification of intrinsic cell spreading in isolated cells ($n = 98$ control and 96 *Srgap2* KD cells; Mann-Whitney test; *** $p < 0.001$; ns, not significant). Scale bars, 40 μm (A and B) and 20 μm (G and J). See also Figures S1 and S2.



(legend on next page)

and GAPs (Figure 6D; Figures S5D and S5E). Expression of the Y40C Rac1 mutant biosensor, in which biosensor distribution is preserved, yielded a flat ER profile (Figures 6E and 6F). This indicates that the biosensor faithfully reports on Rac1 activation dynamics independently of cell geometry. As shown before (Kraynov et al., 2000; Kurokawa et al., 2004), evaluation of Rac1-2G in motile fibroblasts revealed that Rac1 is activated in a broad gradient spanning several micrometers from the protruding cell edge inward the cell (Figures 6G and 6H; Movie S6). Rac1 activity then ceased immediately during edge retraction. Together, the robust spectral properties of this second-generation biosensor reduce phototoxicity and photobleaching and allow for monitoring of Rac1 activity in time and space.

Rac1 Activity Peaks at the Tip of Contact Protrusions

The existence of specific morphodynamics and a specialized F-actin cytoskeleton in contact protrusions suggested distinct modes of spatiotemporal regulation of Rac1 in contact versus contact-free protrusions (Burridge and Wennerberg, 2004; Ridley, 2006). As shown above, evaluation of Rac1-2G in contact-free protrusions revealed broad Rac1 activation gradient diminishing from the cell edge to the cell interior (Figure 7A; Movie S7). In contrast, Rac1 activation was specifically restricted to a focused band at the tip of contact protrusions (Figures 7B and 7C; Movie S8), a pattern reminiscent of both the robust F-actin (Figures 3C–3E) and srGAP2 (Figure 4K) focused bands detected at the same location. Rac1 activity fluctuations at the tip of contact protrusions correlated with protrusion growth and shrinkage (Figures 7D and 7E). Together, these results indicate distinct spatiotemporal Rac1 activation dynamics in contact-free versus contact protrusions that further correlate with their different morphodynamics.

SrGAP2 Specifically Regulates Rac1 Activity in Contact Protrusions

Because srGAP2 bears specific GAP activity toward Rac1 (Guerrier et al., 2009) and because srGAP proteins mediate cell-cell

repulsion in neuronal cells (Wong et al., 2001), we analyzed the impact of *Srgap2* KD on Rac1 activation. Surprisingly, we detected the characteristic Rac1 activity pattern at the tip of contact protrusions in both control and *Srgap2* KD cells. However, while Rac1 activation peaked transiently in control cells, it persisted for longer times in *Srgap2* KD cells (Figure 7F). The tip-restricted Rac1 activity profiles correlated with the above-described contact protrusion dynamics: control protrusions collapsed with decreasing Rac1 activity while *Srgap2* KD protrusions continued to expand in the presence of sustained, focused Rac1 activity (Figures 7G and 7H). In contrast to contact protrusions, *Srgap2* KD did not affect Rac1 activation patterns in contact-free protrusions (Figure 7I). These results show that srGAP2 limits the duration of the tip-restricted Rac1 activity to regulate contact protrusion collapse.

DISCUSSION

By identifying the Slit2-Robo4-srGAP2 signaling system as a spatiotemporal regulator of fibroblast CIL, we link extracellular signaling cues and cell surface molecules to the Rho GTPase-dependent control of cytoskeletal dynamics governing CIL. CIL occurs on an hourly timescale and consists of two phases as follows: (1) a sensing phase leading to protrusion collapse, and (2) a repolarization phase resulting in change of migrational direction. At the timescale of minutes, we find the sensing phase to involve stochastic extension-retraction cycles of specialized contact protrusions, which constantly probe surrounding cells by crawling under the edges of adjacent cells. While displaying identical lifetimes as contact-free protrusions, contact protrusions exhibit increased extension-retraction amplitude, probably to efficiently register repulsive cues in cell-cell overlaps. Contact protrusions display a specific tip-localized, focused F-actin band, which might act as a very robust lamellipodial network that ensures efficient edge extension while squeezing below a neighboring cell. Our analysis also shows that contact-free protrusions in cells with cell-cell overlap are more dynamic and persistent than

Figure 3. SrGAP2 Regulates the Dynamics of Contact, but Not Contact-free, Protrusions

- (A) Rationale for evaluation of contact protrusion geometry. Dashed line indicates ventral cell part detectable with TIRF microscopy, which discriminates attached and non-attached cell edge portions in cell-cell overlaps.
- (B) Composite images of Lifeact-GFP (magenta) and Lifeact-mCherry (cyan) cells with cell-cell overlaps and contact-free edges. EPI and TIRF channels are shown. Black arrowheads depict lamellipodia and filopodia in cell-cell overlaps.
- (C) TIRF images of Lifeact-GFP (left) and Lifeact-mCherry cells (right) shown in inverted black/white colors. Cyan and magenta lines represent outlines of the Lifeact-mCherry and Lifeact-GFP cell, respectively. Red arrowheads denote contact protrusions with the characteristic F-actin band at the leading edge and blue arrowheads depict cell regions, which get displaced from the TIRF field.
- (D) Time series of contact and contact-free protrusions (boxes 1 and 2 in B, respectively). TIRF images of Lifeact-mCherry cell are shown in inverted black-white contrast. Magenta line outlines the Lifeact-GFP cell. Fluorescence signals are scaled identically in both boxes. Timescale, minutes:seconds.
- (E) Line scans of normalized F-actin intensity in contact and contact-free protrusions imaged by TIRF, drawn according to scheme. Graph displays mean \pm SEM; n = 50 protrusions for each condition; two-tailed unpaired Student's t test.
- (F) Kymograph analysis of edge and F-actin dynamics of contact and contact-free protrusions along the yellow lines in (D). Fluorescence signals are scaled identically. Magenta line denotes cell border of the adjacent Lifeact-GFP cell.
- (G–J) Quantification of total cell edge movement (G), edge protrusion (H), edge retraction (I), and net cell edge movement (J) of contact-free and contact protrusions (n = 54 and 76 kymographs of free and contact protrusions, G and J; n \geq 474 and \geq 397 individual protrusions and retractions, respectively, H and I; two-tailed unpaired Student's t test).
- (K–O) Quantification of total cell edge movement (K), net edge movement (L), persistence of movement (M), edge protrusion (N), and edge retraction (O) in contact-free and contact protrusions of control and *Srgap2* KD cells (n = 87, 63, 60, and 63 kymographs, K–M; n \geq 622, 505, 467, and 330 protrusions or retractions, N and O; Bonferroni multiple comparison test).
- (P) Summary of contact-free and contact protrusion dynamics in control and *Srgap2* KD cells. Movement of cell edge is shown in time. Boxplots show median, IQR (box), and outliers (dots). Whiskers represent 1.5 IQR (G, J, and K–M) or extend to minimum and maximum values (H, I, N, and O). **p < 0.01; ***p < 0.001; ns, not significant. Scale bars, 20 μ m (B and C) and 5 μ m (D). See also Figures S1 and S2.

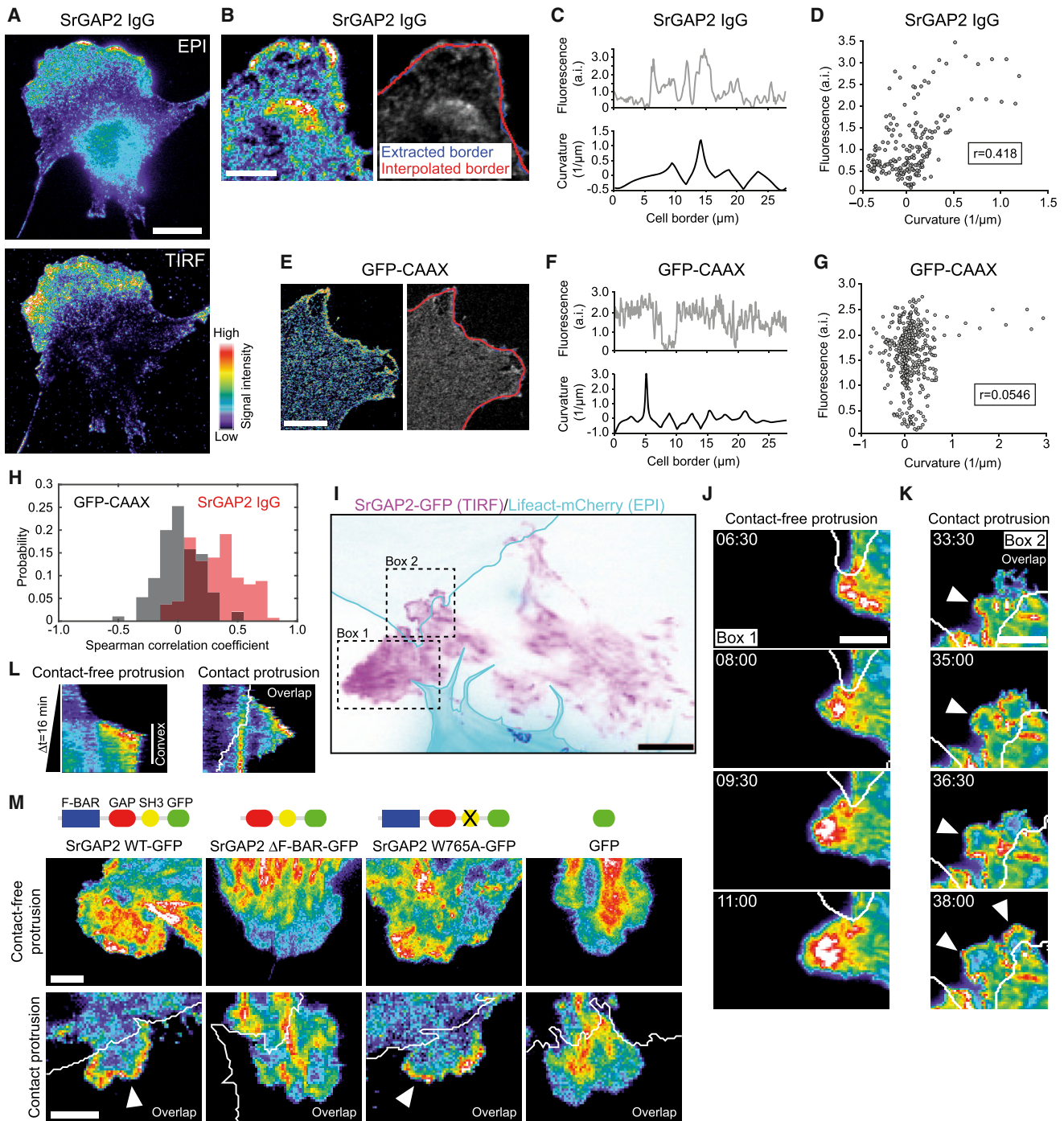


Figure 4. SrGAP2 Dynamically Enriches at the Tip of Contact Protrusions during Their Extension, but Not Retraction, Phase

(A) SrGAP2 immunostaining. TIRF and EPI channels are shown in pseudocolors.

(B) Representative images of single confocal planes of protrusions stained with anti-srGAP2 IgG shown in pseudocolor and black-white contrast. Image was segmented and the cell border was extracted (blue line). Red line represents interpolation of the extracted cell border by third-order polynomial splines.

(C) Fluorescence intensity (gray line) and cell edge curvature (black line) profiles along the cell border in (B) are shown.

(D) Correlation of fluorescence intensity and cell edge curvature obtained from (C). Spearman correlation coefficient is shown in the black box.

(E) Representative pseudocolor and black-white contrast images of protrusions in cells expressing membrane-tethered GFP-CAAX, which were analyzed as in (B).

(F) Fluorescence intensity (gray line) and cell edge curvature (black line) profiles along the cell border in (E) are shown.

(G) Correlation of fluorescence intensity and cell edge curvature obtained from (F). Spearman correlation coefficient is shown in the black box.

(legend continued on next page)

those in isolated cells. This suggests a mechanical cross-talk between the cell-cell overlap zone and contact-free edges that drives the establishment of persistent contact-free protrusions, ultimately enabling cell repolarization and change of migrational direction during CIL. Interestingly, such a redistribution of cellular forces from cell contact regions toward free cell edges has been reported recently to occur during CIL in *Xenopus* neural crest cells (Scarpa et al., 2015).

At the whole-cell scale, srGAP2 loss of function suppresses CIL through abrogation of cell-cell repulsion both in primary and transformed fibroblasts. At the subcellular scale, srGAP2 specifically terminates the extension phase of contact, but not contact-free, protrusions during mutual stochastic sensing. SrGAP2 contains an F-BAR domain that, contrary to other F-BAR domains, has been shown to induce membrane protrusions rather than invaginations when overexpressed as an isolated domain (Guerrier et al., 2009). We show that srGAP2 dynamically binds to convex extending, but dissociates from concave retracting, contact and contact-free protrusions in an F-BAR domain-dependent fashion. The respectively focused and broad srGAP2 distribution in contact and contact-free protrusions might be modulated by differences in cell edge geometry. Thus, the F-BAR domain seems to work as a cell edge geometry-dependent sensor to dynamically tether srGAP2 to extending protrusions, ideally pre-positioning srGAP2 for regulation of protrusions in the eventuality of a cell-cell collision.

The ability of srGAP2 to specifically regulate contact protrusions implies that it receives additional upstream inputs, most likely from the Slit-Robo system, which it interacts with (Wong et al., 2001) and which is expressed in primary and transformed fibroblasts. Consistently, we identify multiple Slit and Robo isoforms to be important for cell-cell repulsion. Furthermore, as for srGAP2, we find that Slit2 and Robo4 are pre-polarized at the ventral membrane of contact-free protrusions in motile fibroblasts. The enrichment of the repulsion machinery at the leading edge provides an elegant explanation for the observation that head-to-head collisions are more efficient in eliciting CIL than head-to-tail collisions, as reported in epithelial cells (Desai et al., 2013) and *Drosophila* hemocytes (Davis et al., 2015), although physical coupling of actin networks was found to constitute the driving force in the latter cell system.

In agreement with their localization pattern, Slit2 and Robo4 mediate CIL in colliding cells. Importantly, Slit2 and Robo4 have been found to function as a cognate ligand-receptor system in endothelial cells (Jones et al., 2008). Slit molecules interact with HSPGs (Ypsilanti et al., 2010). Thus, Slit2 may be presented to Robo4 in a glycocalyx-tethered form in cell-cell

overlaps, which remains to be investigated. Although we do not formally show that physical interaction between overlapping membranes occurs, the fact that depletion of Slit2 or Robo4 impairs CIL strongly suggests that repulsive signals are transferred between cells in cell-cell overlaps, rather than through long-range Slit secretion.

SrGAP2 is a specific GAP for Rac1 (Guerrier et al., 2009). Intriguingly, we find two distinct spatiotemporal Rac1 activation patterns in contact and contact-free protrusions. As shown before (Kurokawa et al., 2004), we detect a broad Rac1 activation gradient in contact-free protrusions. In contrast, Rac1 activity is concentrated in a narrow band at the tip of contact protrusions. We propose that it might regulate the robust lamellipodial F-actin pool, which also is present at this specific location. The differences in Rac1 activity patterns in contact-free versus contact protrusions within the same cell suggest that different GEFs and GAPs may be required to fine-tune the actin cytoskeleton to yield context-dependent morphodynamics. This extends recent findings of context-dependent spatiotemporal Rho GTPase activation programs in response to different extracellular cues (Kutys and Yamada, 2014; Martin et al., 2014; Pertz et al., 2006).

Unintuitively, srGAP2 loss of function leads to increased protrusion extension without affecting the characteristic, narrow Rac1 activity band itself. This suggests that an additional GEF-GAP signaling network shapes this specific subcellular Rac1 activation pattern through a reaction-diffusion system (Bement and von Dassow, 2014). The fact that srGAP2 colocalizes with active Rac1 during contact protrusion extension necessitates that its GAP activity is not constitutively active. In agreement, srGAP proteins are held in an auto-inhibited conformation through interaction between their N and C termini, which might get relieved through interactions between the SH3 domain and its cognate ligands (Guerrier et al., 2009; Zaidel-Bar et al., 2010). We therefore speculate that srGAP2 controls the duration of the Rac1 activation band by integrating cell geometry inputs through its F-BAR domain and repulsive inputs from a Robo receptor by its SH3 domain (Wong et al., 2001). This might provide an elegant spatiotemporal signaling mechanism to both position and activate the Slit-Robo repulsive machinery in contact protrusions during cell-cell collisions. Additional repulsive systems are likely to fine-tune mesenchymal cell interactions through control of Rho GTPases (Astin et al., 2010; Sugiyama et al., 2013; Carmona-Fontaine et al., 2008; Huttenlocher et al., 1998; Matthews et al., 2008; Takai et al., 2008; Scarpa et al., 2015; Theveneau et al., 2010), and it will be important to decipher if similar spatiotemporal Rho GTPase mechanisms occur in those signaling systems during CIL.

(H) Distribution of Spearman correlation coefficients of signal intensity and cell edge curvature for cells immunostained for srGAP2 (red bars) or exogenously expressing GFP-CAAX (gray bars) are shown ($n = 120$ protrusions [srGAP2] and $n = 95$ protrusions [GFP-CAAX]).

(I) Composite TIRF/EPI image of a srGAP2-GFP-expressing cell (magenta) during infiltration beneath a cell expressing Lifeact-mCherry (cyan). Cyan lines indicate the outline of Lifeact-mCherry cells.

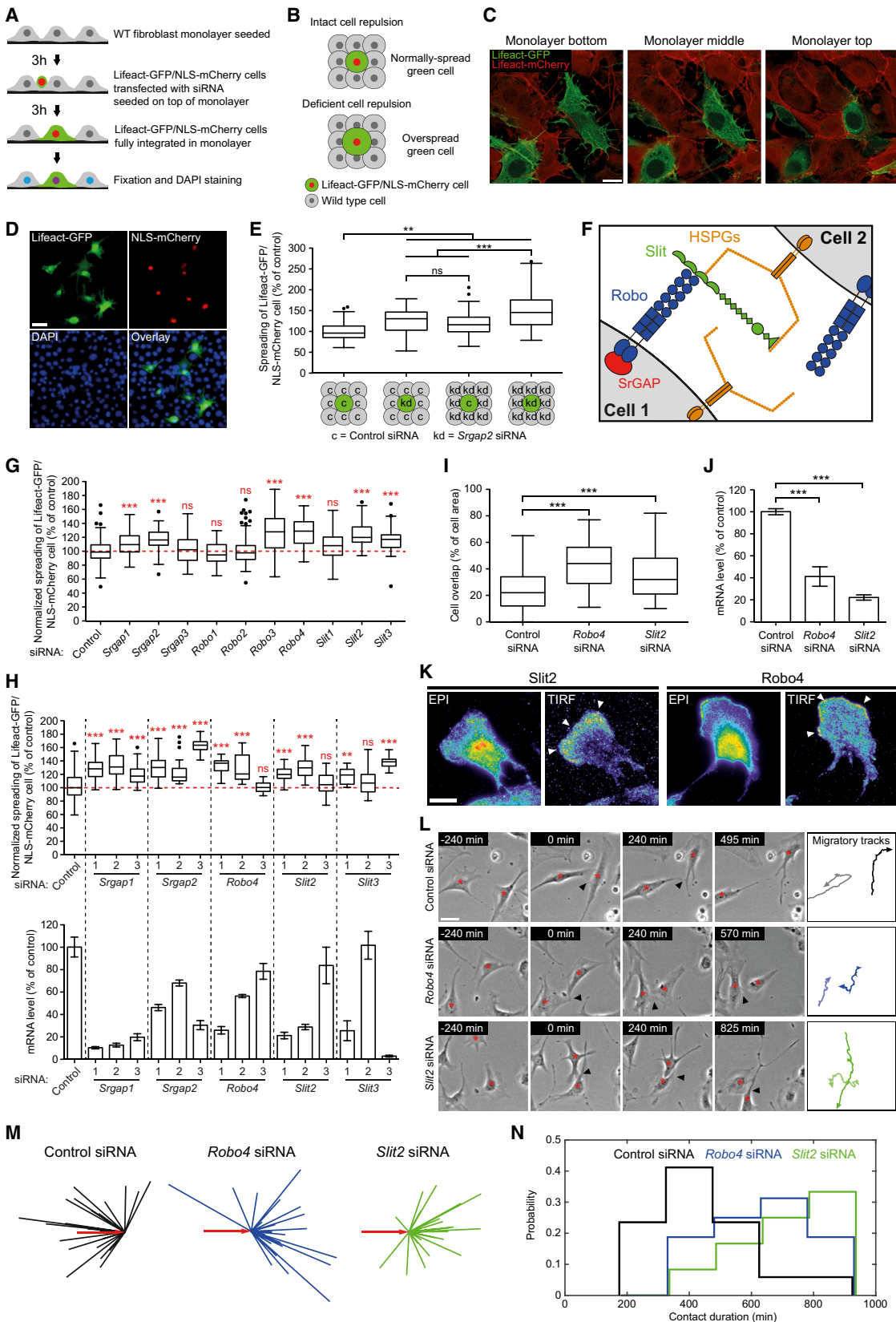
(J) Time series shows contact-free protrusion from box 1 in (I).

(K) Time series of contact protrusion from box 2 in (I). White arrowheads designate highly focused srGAP2 accumulation at the cell edge.

(L) Kymograph analysis of srGAP2 dynamics in contact-free and contact protrusions. White line depicts cell border and defines the overlap region.

(M) Subcellular dynamics of exogenously expressed srGAP2 mutants in contact-free and contact protrusions analyzed by TIRF microscopy. White lines indicate cell-cell overlaps. White arrowheads point toward srGAP2 enrichment.

Scale bars, 20 μm (A), 5 μm (B and J–M), and 10 μm (E and I). See also Figures S3 and S4.



(legend on next page)

EXPERIMENTAL PROCEDURES

Characterization of Rac1 FRET Biosensors by Fluorometry and Microscopy

Analysis of the fluorescence emission spectra of the Rac1 sensor library, the different Rac1-2G mutants, as well as Rac1-2G's responses to GEFs and GAPs were performed on a fluorometer (Perkin Elmer LS50b). Typically, 2×10^5 HEK293FT cells were seeded into a 12-well cell culture plate and transfected with 100 ng biosensor, 400 ng RhoGDI or GAPs, and 1,000 ng GEFs using Metafectene (Biontex). After 48 hr, cells were detached with brief trypsin treatment and resuspended in ice-cold PBS and cell suspensions were transferred into a quartz cuvette. Rac1-2G was excited at 460 nm and emission spectra were recorded from 480 to 600 nm with a step of 0.5 nm. Spectra were background-subtracted with spectra of non-transfected cells and normalized according to their spectrum integral. Relative FRET was calculated by dividing the normalized fluorescence intensity of Venus at its emission peak (528 nm) by the normalized fluorescence intensity of mTFP1 at its emission peak (492 nm).

Additionally, the impact of GEFs and GAPs on the Rac1-2G biosensor was measured by microscopy. Here, HEK293FT cells were transfected as described above, were seeded into a 96-well plate (Falcon) coated with 10 $\mu\text{g}/\text{mL}$ PLL, and nine fields of view were acquired per experiment using a Plan Apo 10 \times objective and the Screening Acquisition Module in MetaMorph (Molecular Devices). The average ratio per field of view was then calculated from ≥ 100 cells.

Microscopy Settings and Live-Cell Imaging

Epifluorescence and TIRF microscopy were performed on a Nikon Ti Eclipse inverted microscope equipped with a motorized stage, hardware-based autofocus, and a TIRF module containing 491- and 561-nm solid-state lasers (Roper Scientific). MetaMorph (Molecular Devices) was used to control the microscope; 440-, 470-, and 565-nm LEDs (CoolLED) were used as light sources in the epifluorescence imaging regime. Images were acquired with an Orca R2 CCD camera (Hamamatsu) at 16-bit depth. Epifluorescence images were acquired using 10 \times Plan Apo and 60 \times Plan Apo VC objectives at binning 2 \times 2. TIRF images were recorded using a 60 \times Plan Apo TIRF objective. Live-cell imaging was performed at 37°C in Ham's F12 medium (Gibco) supplemented with 2% fetal bovine serum (FBS), 4 mM L-Glutamine, and 100 U/ml

penicillin/streptomycin. Filter sets (Chroma) were as follows: ET470/40x-59022bs-ET525/50 m (GFP); ET572/35x-59022bs-ET632/60 m (mCherry); ET572/35x-59006bs-ET632/60 m (mCherry combined with FRET imaging); 430/24x-Q465L-ET480/40 m (mTFP1); 430/24x-Q465L-ET535/30 m (FRET); and ET402/15x-89100bs-ET455/50 m (DAPI). Confocal imaging was performed on a Zeiss LSM 510 Meta scanning microscope. Images were adjusted for brightness and contrast only using MetaMorph (Molecular Devices).

Ratiometric FRET Imaging and Image Processing

FRET imaging was performed as described previously (Fritz et al., 2013). Briefly, NIH 3T3 cells infected with the Rac1 FRET biosensor were mixed with Lifeact-mCherry cells and seeded subconfluently to detect contact and contact-free protrusions in one sample. To assess the impact of srGAP2 KD on Rac1 activation, we used NIH 3T3 cells stably expressing control or Srgap2 shRNAs instead of siRNA-transfected cells to lower cell toxicity. Cells expressing low levels of the sensor were acquired with a 60 \times Plan Apo TIRF or 60 \times Plan Apo VC objective at binning 4 \times 4 and 2-min time resolution. Donor and FRET images were acquired sequentially with exposure times ≤ 300 ms. Processing of epifluorescence ratiometric datasets was performed with the Biosensor Processing Software 2.1 (Danuser laboratory: <http://lccb.hms.harvard.edu/software.html>). Subsequent image analysis was performed in MetaMorph (Molecular Devices). Ratio images are color-coded so that warm and cold colors represent high and low biosensor activity, respectively. The distribution of the biosensor was monitored in the donor channel. To visualize cell-cell overlap regions, borders of Lifeact-mCherry cells were generated based on binary images of the mCherry channel (Laplace1 function in MetaMorph [Molecular Devices]).

Analysis and Quantification of CIL

CIL assays were started 48 hr after transfection of NIH 3T3 cells or primary MEFs with siRNAs. Cells (7×10^4) were seeded per well of a six-well plate and allowed to adhere on glass coated with 5 $\mu\text{g}/\text{ml}$ fibronectin for 3 hr in DMEM supplemented with 10% FBS, 4 mM L-Glutamine, and 100 U/ml penicillin/streptomycin. Phase-contrast images subsequently were acquired for 20 hr on a Nikon Ti Eclipse inverted microscope with a 10 \times Plan Fluor objective. Cell nuclei were tracked using MetaMorph (Molecular Devices) software. Cells were tracked for equal time periods before and after cell-cell collision to yield two vectors that allowed for quantification of the migrational direction.

Figure 5. The Slit-Robo Pathway Mediates Cell-Cell Repulsion in Fibroblasts, Localizes to Contact-free Protrusions, and Regulates CIL

- (A) Outline of the monolayer integration assay used for siRNA screening.
 - (B) Rationale for evaluation of contact-dependent cell-spreading phenotypes in the monolayer integration assay. Possible outcomes of cell contact-dependent spreading phenotypes are shown.
 - (C) Confocal images show the cell monolayer taken 3 hr after seeding of Lifeact-GFP cells atop the Lifeact-mCherry monolayer.
 - (D) EPI images of Lifeact-GFP-NLS-mCherry cells embedded within a monolayer of WT cells. Monolayer integrity and density was evaluated using the DAPI channel.
 - (E) Average spreading of control and Srgap2 KD cells in confluent monolayers is shown ($n = 58, 63, 59$, and 62 fields of view; Bonferroni multiple comparison test).
 - (F) Schematic depiction of the Slit-Robo signaling pathway. The soluble ligand Slit is captured by HSPGs at the cell surface and presented to Robo receptors. The repulsive signal is further transduced via srGAP proteins to small Rho family GTPases.
 - (G) Quantification of contact-dependent spreading of Lifeact-GFP-NLS-mCherry cells embedded within monolayer cultures and treated with the indicated siRNA pools. Average spreading of multiple Lifeact-GFP-NLS-mCherry cells in one field of view was measured ($n = 193, 92, 50, 70, 97, 74, 73, 57, 57, 52, 58, 76$, and 73 fields of view; Bonferroni multiple comparison test).
 - (H) Quantification of contact-dependent spreading of Lifeact-GFP-NLS-mCherry cells embedded within monolayer cultures and treated with the indicated individual siRNAs (top; $n = 46, 34, 31, 46, 41, 34, 29, 29, 35, 39, 36, 37, 41, 29, 42$, and 29 fields of view) and their respective knockdown efficiencies (bottom; mean \pm SD; $n = 2$ measurements). Spreading analysis was performed as in (G). Bonferroni multiple comparison test.
 - (I) Quantification of cell-cell overlap of Lifeact-GFP cells transfected with siRNA pools and grown in Lifeact-mCherry monolayers is shown ($n = 135, 86$, and 101 cells; Dunn's multiple comparison test).
 - (J) Knockdown efficiency of Robo4 and Slit2 siRNA pools as measured by qPCR is shown (mean \pm SEM; $n = 4$ measurements; Bonferroni multiple comparison test).
 - (K) Immunostaining for Slit2 and Robo4. TIRF and EPI channels are shown in pseudocolors. White arrowheads denote enrichment of these proteins at the leading edge.
 - (L) Phase-contrast time series of control and Robo4 and Slit2 KD cells treated with siRNA pools during cell collision. Migration trajectories are summarized (right). Black arrowheads designate contacts between cell edges. Timescale, minutes.
 - (M) Scaled cell-displacement vectors of colliding cells as in Figure 2E are shown ($n = 22$ control, 24 Robo4 KD, and 23 Slit2 KD cells).
 - (N) Distribution of cell-cell contact duration ($n = 17, 13$, and 17 collisions of control, Robo4, and Slit2 KD cells, respectively).
- Boxplots show median, IQR (box), 1.5 IQR (whiskers), and outliers (dots). ** $p < 0.01$, *** $p < 0.001$; ns, not significant. Scale bars, 10 μm (C), 20 μm (K), 40 μm (L), and 50 μm (D). See also Figure S1.

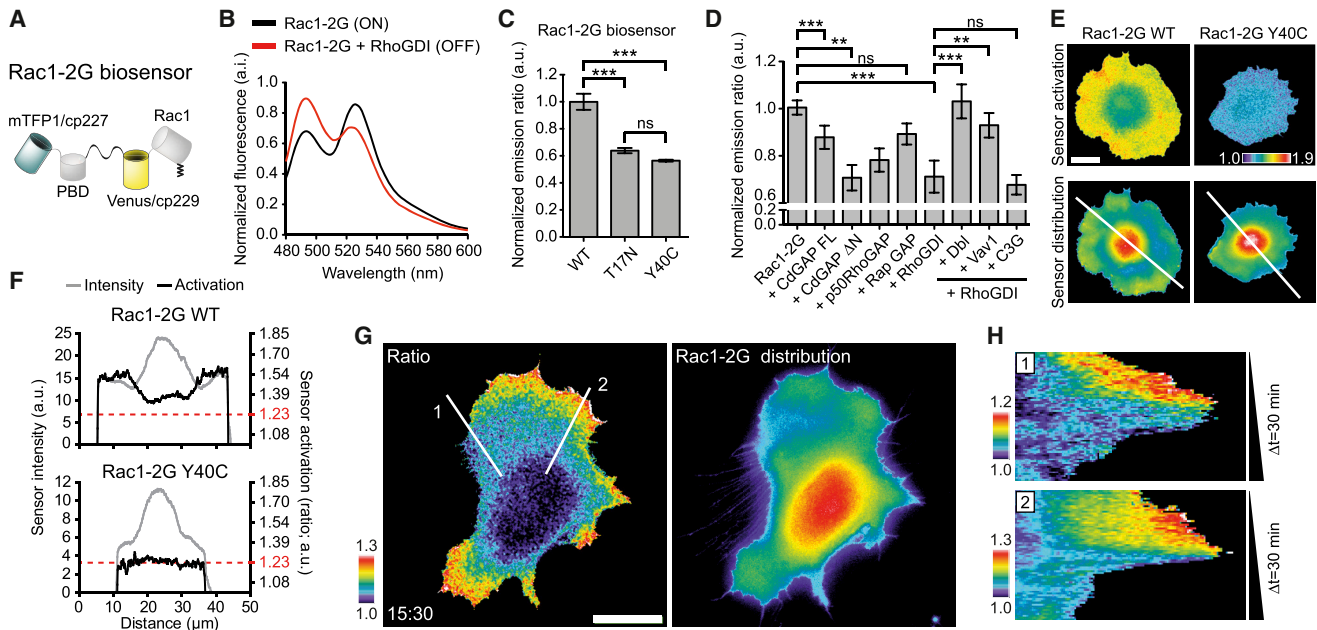


Figure 6. Construction and Characterization of a Single-Chain, Genetically Encoded Rac1 FRET Biosensor

- (A) Rac1-second generation (Rac1-2G) biosensor architecture. A PAK1-binding domain (PBD) is used to sense Rac1 nucleotide loading status. Rac1-2G contains circular permutation (cp) 227 of monomeric Teal fluorescent protein 1 (mTFP1; FRET donor) and cp229 of Venus (FRET acceptor).
- (B) Fluorescence spectrum of active and inactive Rac1 sensor. HEK293FT cells were transfected with Rac1-2G alone (ON state) or in presence of RhoGDI (OFF state) and measured using fluorometry. Spectrum was normalized by the area under the curve.
- (C) Evaluation of Rac1-2G biosensor mutants in HEK293FT cells by fluorometry is shown ($n = 3$ experiments; Bonferroni multiple comparison test).
- (D) Evaluation of Rac1-2G in response to coexpression of upstream regulators in HEK293FT cells using fluorometry. Full-length CdGAP (CdGAP FL) and the constitutively active, truncated CdGAP (CdGAP Δ N) can act as Rac1 GAP (Lamarche-Vane and Hall, 1998). p50RhoGAP is a GAP for Rac1, Cdc42, and RhoA, while Rap GAP is Rap1 specific. Dbl and Vav1 are Rac1-specific GEFs, while C3G is a Rap1-specific GEF ($n \geq 2$ experiments; Bonferroni multiple comparison test).
- (E) Evaluation of WT and Y40C mutant Rac1-2G ER in REF52 fibroblasts. Rac1-2G activation (top) and distribution (mTFP1 channel; bottom) are shown.
- (F) Fluorescence intensity and ER profiles across lines shown in (E). ERs are scaled identically in both cells.
- (G) Analysis of Rac1 activation patterns (ratio) in REF52 fibroblasts stimulated with 40 ng/ml platelet-derived growth factor. Biosensor distribution is shown in the FRET channel.
- (H) Kymograph analysis of Rac1 activation dynamics during edge extension/retraction measured along lines in (G).
- Scale bars, 40 μm (E) and 20 μm (G). See also Figures S5 and S6.

Cell displacement vectors are presented as in Carmona-Fontaine et al. (2008). The length of vectors before collision was normalized and vectors aligned. The length of each post-collision vector was scaled accordingly to show the relative cell displacement after cell-cell collision. Contact time was determined based on images taken in 15-min steps.

Single-Cell Migration and Wound-Healing Assay

All cell migration assays were performed 48 hr post-transfection with siRNAs. For single-cell migration, 1.5×10^2 NIH 3T3 Lifeact-GFP/nuclear localization sequence (NLS)-mCherry cells transfected with siRNAs were seeded per well of a culture insert (80209, Ibidi) mounted on 24-mm glass coverslips coated with 5 μg/ml fibronectin. Cells were allowed to adhere for 3 hr in DMEM supplemented with 10% FBS, 4 mM L-Glutamine, and 100 U/ml penicillin/streptomycin before removal of the culture insert and imaging. For wound-healing assays, 3×10^3 NIH 3T3 Lifeact-GFP/NLS-mCherry cells transfected with siRNAs were mixed with 1.2×10^4 untransfected NIH 3T3 WT cells and seeded into one chamber of a culture insert (80209, Ibidi) mounted on 24-mm glass coverslips coated with 5 μg/ml fibronectin. Cells were allowed to adhere for 3 hr in DMEM supplemented with 10% FBS, 4 mM L-Glutamine, and 100 U/ml penicillin/streptomycin before removing the culture insert and introducing a scratch wound with a pipette tip. Cells were imaged in Ham's F12 medium (Gibco) supplemented with 2% FBS, 4 mM L-Glutamine, and 100 U/ml penicillin/streptomycin on a Nikon Ti Eclipse inverted microscope with a 10x Plan Fluor objective. Transmitted light

(binning 2×2) and mCherry (binning 8×8) channels were recorded. A 10 × 10 low-pass filter was applied to the mCherry channel to increase signal-to-noise ratio and nuclei were tracked using MetaMorph (Molecular Devices) software. Accumulated travel distance and directional persistence were calculated with the Chemotaxis and Migration Tool 2.0 (Ibidi), and migratory tracks were generated with Origin 8 software (OriginLab).

Cell Contact-Dependent Cell-Spreadng Assay

To measure contact-dependent cell spreading, 1.5×10^5 untransfected NIH 3T3 WT cells were seeded in DMEM supplemented with 10% FBS, 4 mM L-Glutamine, and 100 U/ml penicillin/streptomycin (complete medium) into a 24-well plate (Genetix) coated with 5 μg/ml fibronectin. Cells were centrifuged at $200 \times g$ for 2 min at room temperature and allowed to form a monolayer for 3 hr at 37°C. Subsequently, the monolayer was rinsed three times with complete medium and 3×10^4 Lifeact-GFP/NLS-mCherry cells transfected with siRNAs were seeded atop the monolayer and cultured for 3 hr in complete medium at 37°C. In parallel, 5×10^3 siRNA-treated Lifeact-GFP/NLS-mCherry cells were sparsely seeded to assess the impact of each siRNA on intrinsic cell spreading. The monolayer was then rinsed three times with PBS to remove non-integrated Lifeact-GFP/NLS-mCherry cells and fixed in parallel with the isolated cells in 4% paraformaldehyde for 10 min at room temperature. All cells were stained with DAPI (Molecular Probes). GFP, mCherry, and DAPI images of ~ 500 cells per field of view were acquired using the Screening Acquisition Module in MetaMorph (Molecular Devices). Per condition and experiment,

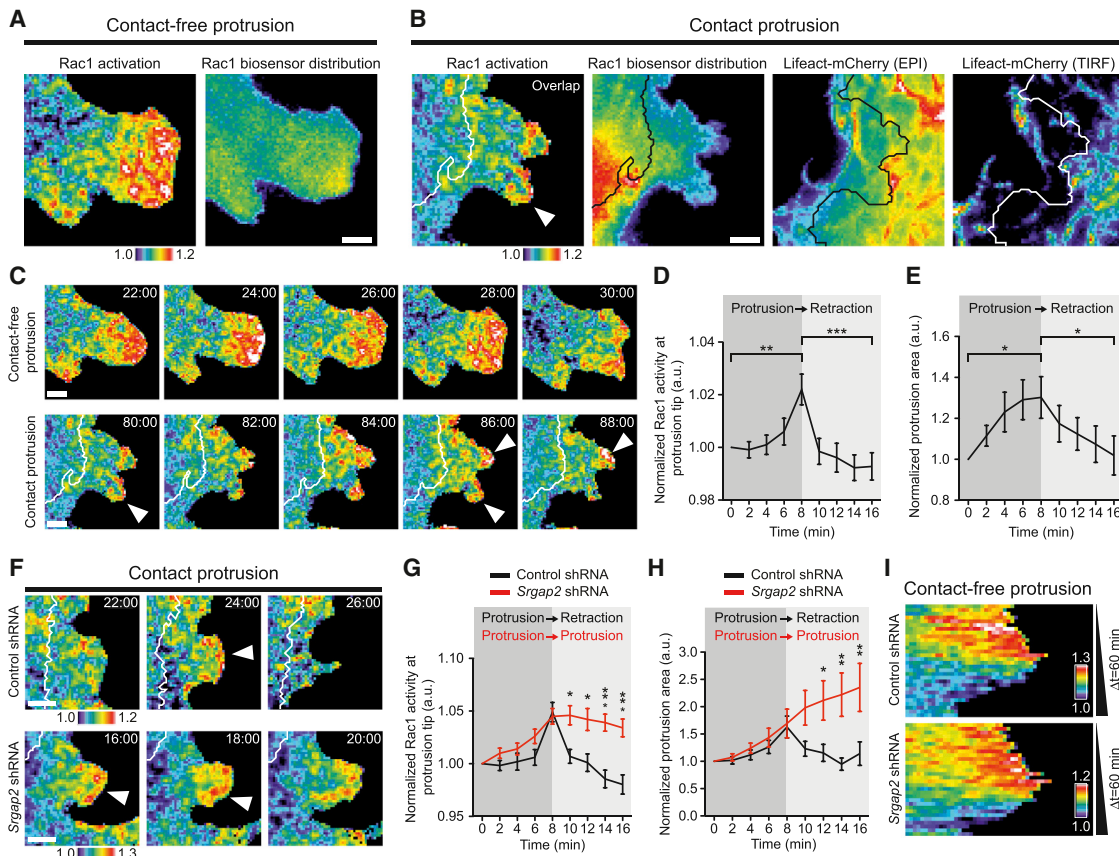


Figure 7. SrGAP2-Dependent Rac1 Activation Dynamics in Contact Protrusions

(A) Rac1 activation in contact-free protrusions. Rac1 activation (ratio) and biosensor localization (mTFP1 channel) are shown. Warm and cold colors represent high and low Rac1 activation/distribution, respectively.

(B) Rac1 activation in contact protrusions. Lifeact-mCherry neighboring cells are shown in pseudocolor in EPI and TIRF images. White or black lines define cell-cell overlap regions according to the Lifeact-mCherry channel. White arrowhead denotes spatially restricted Rac1 activation at the cell edge.

(C) Time series of contact-free protrusions from (A) and contact protrusions from (B). Ratio scaling is identical as in (A) and (B). White arrowheads denote transient focused Rac1 activation bands.

(D and E) Quantification of Rac1 activity at the tip of contact protrusions (D) and contact protrusion size (E). Graphs represent mean \pm SEM; $n = 33$ protrusion events from 11 cells; Dunn's multiple comparison test.

(F) Time series of Rac1 activation dynamics in control and Srgap2 KD cells stably expressing shRNAs. White arrowheads indicate focused Rac1 activity.

(G and H) Quantification of Rac1 activity (G) at the tip of contact protrusion and contact protrusion size (H) in control and Srgap2 KD cells ($n = 26$ and 24 protrusive events measured in ten control and six Srgap2 KD cells, respectively). Graph shows mean \pm SEM. Dunn's multiple comparison test was used to compare between shRNAs.

(I) Kymograph analysis of Rac1 activation dynamics in contact-free protrusions in control and Srgap2 KD cells is shown.

All timescales, minutes:seconds. All scale bars, 5 μ m. * $p < 0.05$, ** $p < 0.01$, *** $p < 0.001$.

64 fields of view were recorded, and only fields of view with similar numbers of DAPI-positive cells were considered for analysis to obtain similar cell densities. Total cell surface per field of view was measured in the GFP channel and divided by the number of NLS-mCherry-positive cells to obtain an average cell spreading per field of view. Contact-dependent spreading in the monolayer was normalized by cell spreading of sparse cells to correct for the effect of siRNA treatment on intrinsic cell spreading.

Correlation Analysis of Cell Edge Curvature and srGAP2 Amount at the Cell Edge

We calculated a correlation coefficient for the local curvature of the cell edge and the intensity of the fluorescent signal at the cell edge in that point. To this end, we developed a MATLAB-based pipeline, which includes the following steps (Figure S3): image segmentation, boundary extraction, calculation of the boundary curvature, readout of fluorescent signal intensity at the cell boundary, and correlation analysis of curvature and intensity. Single-plane

confocal images were segmented based on the image intensity gradient. The boundary of the cell was then extracted with the MATLAB function bwboundaries. Points that belong to the border of the acquired image were eliminated from the cell boundary. The longest continuous curve representing cell boundary, β was parameterized in the following way: $\beta(x, y) = \beta(x(i), y(i))$, where $x(i)$ and $y(i)$ are x and y coordinates of the i th pixel along the border. This discrete parameterization β was fitted with the third-order polynomial spline (spap2 MATLAB function) to obtain a smooth parameterization $\bar{\beta} = \bar{\beta}(\bar{x}(t), \bar{y}(t))$. The third-order polynomial spline was chosen to ensure continuity of the second-order derivatives of the parameterization, necessary to calculate curvature. The number of pixels fitted with one spline was typically set to 20. Finally, curvature was calculated according to the formula

$$\kappa = \frac{x'y'' - y'x''}{(x'^2 + y'^2)^{3/2}}$$

where ' denotes derivative. Image intensity was read out from the nearest pixel along the smooth border $\bar{\beta}$. The Spearman correlation coefficient (corr MATLAB function) was then calculated between the extracted image intensity at boundary and the cell edge curvature.

For time-lapse data, TIRF images were preliminarily segmented with a threshold-based filter (im2bw MATLAB function). The preliminarily segmented images were used as a mask for an active contour segmentation (activecontour MATLAB function).

Statistical Analysis

Statistical analysis was conducted with Prism5 software (GraphPad). D'Agostino and Pearson omnibus normality test was used to check for Gaussian distribution before comparing groups. Datasets containing two groups were analyzed by two-tailed, unpaired Student's t test (Gaussian distribution) or by Mann-Whitney test (non-Gaussian distribution). Datasets composed of three and more groups were analyzed by one-way ANOVA followed by Bonferroni multiple comparison tests (Gaussian distribution) or by Dunn's multiple comparison tests (non-Gaussian distribution). Sample sizes of sufficient power were chosen based on similar published research. Experiments were not randomized and investigators were not blinded. Statistical significant differences are reported at * $p < 0.05$, ** $p < 0.01$, and *** $p < 0.001$.

ACCESSION NUMBERS

The accession numbers for the three biosensor constructs reported in this paper are Addgene: 66110 (pTriEx-Rac1-2G), 66111 (pLenti-Rac1-2G), and 66112 (pAd/CMV/V5-DEST-Rac1-2G).

SUPPLEMENTAL INFORMATION

Supplemental Information includes Supplemental Experimental Procedures, six figures, and eight movies and can be found with this article online at <http://dx.doi.org/10.1016/j.devcel.2015.09.002>.

AUTHOR CONTRIBUTIONS

R.D.F. and O.P. conceived the project and wrote the paper. R.D.F. conducted most experiments. D.M. developed computational tools and performed correlation analysis and quantification of cell edge dynamics. K.M. performed FRET experiments and created stable cell lines. V.P. performed wound-healing and single-cell migration experiments. A.R. constructed and characterized the Rac1 FRET biosensor.

CONFLICTS OF INTEREST

D.M. is an employee of Bayer Technology Systems.

ACKNOWLEDGMENTS

We are grateful to G. Bokoch, X. Bustelo, L. Fusco, A. Howe, M. Kaeser, N. Lamarche-Vane, F. Polleux, J. de Rooij, M. Schwartz, and R. Zeller for sharing reagents. We also thank A. Erni and G. Roest for technical assistance. This work was supported by grants from the Swiss Cancer League and the Swiss National Science Foundation to O.P., University of Basel postdoctoral fellowship to R.D.F., and University of Verona Cooperint grant to V.P.

Received: March 11, 2015

Revised: August 6, 2015

Accepted: September 9, 2015

Published: October 1, 2015

REFERENCES

- Abercrombie, M., and Heaysman, J.E. (1953). Observations on the social behaviour of cells in tissue culture. I. Speed of movement of chick heart fibroblasts in relation to their mutual contacts. *Exp. Cell Res.* 5, 111–131.
- Abercrombie, M., and Heaysman, J.E. (1954). Observations on the social behaviour of cells in tissue culture. II. Monolayering of fibroblasts. *Exp. Cell Res.* 6, 293–306.
- Astin, J.W., Batson, J., Kadir, S., Charlet, J., Persad, R.A., Gillatt, D., Oxley, J.D., and Nobes, C.D. (2010). Competition amongst Eph receptors regulates contact inhibition of locomotion and invasiveness in prostate cancer cells. *Nat. Cell Biol.* 12, 1194–1204.
- Bement, W.M., and von Dassow, G. (2014). Single cell pattern formation and transient cytoskeletal arrays. *Curr. Opin. Cell Biol.* 26, 51–59.
- Burridge, K., and Wennerberg, K. (2004). Rho and Rac take center stage. *Cell* 116, 167–179.
- Carmona-Fontaine, C., Matthews, H.K., Kuriyama, S., Moreno, M., Dunn, G.A., Parsons, M., Stern, C.D., and Mayor, R. (2008). Contact inhibition of locomotion in vivo controls neural crest directional migration. *Nature* 456, 957–961.
- Charrier, C., Joshi, K., Coutinho-Budd, J., Kim, J.E., Lambert, N., de Marchena, J., Jin, W.L., Vanderhaeghen, P., Ghosh, A., Sassa, T., and Polleux, F. (2012). Inhibition of SRGAP2 function by its human-specific paralogs induces neoteny during spine maturation. *Cell* 149, 923–935.
- Davis, J.R., Luchici, A., Mosis, F., Thackery, J., Salazar, J.A., Mao, Y., Dunn, G.A., Betz, T., Miodownik, M., and Stramer, B.M. (2015). Inter-cellular forces orchestrate contact inhibition of locomotion. *Cell* 161, 361–373.
- Dennis, M.Y., Nuttle, X., Sudmant, P.H., Antonacci, F., Graves, T.A., Nefedov, M., Rosenfeld, J.A., Sajadian, S., Malig, M., Kotkiewicz, H., et al. (2012). Evolution of human-specific neural SRGAP2 genes by incomplete segmental duplication. *Cell* 149, 912–922.
- Desai, R.A., Gopal, S.B., Chen, S., and Chen, C.S. (2013). Contact inhibition of locomotion probabilities drive solitary versus collective cell migration. *J. R. Soc. Interface* 10, 20130717.
- Fengos, G., Schmidt, A., Martin, K., Fluri, E., Aebersold, R., Iber, D., and Pertz, O. (2014). Spatial proteomic and phospho-proteomic organization in three prototypical cell migration modes. *Proteome Sci.* 12, 23.
- Fritz, R.D., Letzelter, M., Reimann, A., Martin, K., Fusco, L., Ritsma, L., Ponsioen, B., Fluri, E., Schulte-Merker, S., van Rheenen, J., and Pertz, O. (2013). A versatile toolkit to produce sensitive FRET biosensors to visualize signaling in time and space. *Sci. Signal.* 6, rs12.
- Frost, A., Perera, R., Roux, A., Spasov, K., Destaing, O., Egelman, E.H., De Camilli, P., and Unger, V.M. (2008). Structural basis of membrane invagination by F-BAR domains. *Cell* 132, 807–817.
- Frost, A., Unger, V.M., and De Camilli, P. (2009). The BAR domain superfamily: membrane-molding macromolecules. *Cell* 137, 191–196.
- Guerrier, S., Coutinho-Budd, J., Sassa, T., Gresset, A., Jordan, N.V., Chen, K., Jin, W.L., Frost, A., and Polleux, F. (2009). The F-BAR domain of srGAP2 induces membrane protrusions required for neuronal migration and morphogenesis. *Cell* 138, 990–1004.
- Heasman, S.J., and Ridley, A.J. (2008). Mammalian Rho GTPases: new insights into their functions from in vivo studies. *Nat. Rev. Mol. Cell Biol.* 9, 690–701.
- Huttenlocher, A., Lakonishok, M., Kinder, M., Wu, S., Truong, T., Knudsen, K.A., and Horwitz, A.F. (1998). Integrin and cadherin synergy regulates contact inhibition of migration and motile activity. *J. Cell Biol.* 141, 515–526.
- Jones, C.A., London, N.R., Chen, H., Park, K.W., Sauvaget, D., Stockton, R.A., Wythe, J.D., Suh, W., Larrieu-Lahargue, F., Mukouyama, Y.S., et al. (2008). Robo4 stabilizes the vascular network by inhibiting pathologic angiogenesis and endothelial hyperpermeability. *Nat. Med.* 14, 448–453.
- Kraynov, V.S., Chamberlain, C., Bokoch, G.M., Schwartz, M.A., Slabaugh, S., and Hahn, K.M. (2000). Localized Rac activation dynamics visualized in living cells. *Science* 290, 333–337.
- Kurokawa, K., Itoh, R.E., Yoshizaki, H., Nakamura, Y.O., and Matsuda, M. (2004). Coactivation of Rac1 and Cdc42 at lamellipodia and membrane ruffles induced by epidermal growth factor. *Mol. Biol. Cell* 15, 1003–1010.
- Kutys, M.L., and Yamada, K.M. (2014). An extracellular-matrix-specific GEF-GAP interaction regulates Rho GTPase crosstalk for 3D collagen migration. *Nat. Cell Biol.* 16, 909–917.

- Lamarche, N., Tapon, N., Stowers, L., Burbelo, P.D., Aspenström, P., Bridges, T., Chant, J., and Hall, A. (1996). Rac and Cdc42 induce actin polymerization and G1 cell cycle progression independently of p65PAK and the JNK/SAPK MAP kinase cascade. *Cell* 87, 519–529.
- Lamarche-Vane, N., and Hall, A. (1998). CdGAP, a novel proline-rich GTPase-activating protein for Cdc42 and Rac. *J. Biol. Chem.* 273, 29172–29177.
- Li, X., Chen, Y., Liu, Y., Gao, J., Gao, F., Bartlam, M., Wu, J.Y., and Rao, Z. (2006). Structural basis of Robo proline-rich motif recognition by the srGAP1 Src homology 3 domain in the Slit-Robo signaling pathway. *J. Biol. Chem.* 281, 28430–28437.
- Machacek, M., Hodgson, L., Welch, C., Elliott, H., Pertz, O., Nalbant, P., Abell, A., Johnson, G.L., Hahn, K.M., and Danuser, G. (2009). Coordination of Rho GTPase activities during cell protrusion. *Nature* 461, 99–103.
- Martin, K., Vilela, M., Jeon, N.L., Danuser, G., and Pertz, O. (2014). A growth factor-induced, spatially organizing cytoskeletal module enables rapid and persistent fibroblast migration. *Dev. Cell* 30, 701–716.
- Matthews, H.K., Marchant, L., Carmona-Fontaine, C., Kuriyama, S., Larraín, J., Holt, M.R., Parsons, M., and Mayor, R. (2008). Directional migration of neural crest cells in vivo is regulated by Syndecan-4/Rac1 and non-canonical Wnt signaling/RhoA. *Development* 135, 1771–1780.
- Mayor, R., and Carmona-Fontaine, C. (2010). Keeping in touch with contact inhibition of locomotion. *Trends Cell Biol.* 20, 319–328.
- Nalbant, P., Hodgson, L., Kraynov, V., Touschkin, A., and Hahn, K.M. (2004). Activation of endogenous Cdc42 visualized in living cells. *Science* 305, 1615–1619.
- Pertz, O. (2010). Spatio-temporal Rho GTPase signaling - where are we now? *J. Cell Sci.* 123, 1841–1850.
- Pertz, O., Hodgson, L., Klemke, R.L., and Hahn, K.M. (2006). Spatiotemporal dynamics of RhoA activity in migrating cells. *Nature* 440, 1069–1072.
- Pertz, O.C., Wang, Y., Yang, F., Wang, W., Gay, L.J., Gristenko, M.A., Clauss, T.R., Anderson, D.J., Liu, T., Auberry, K.J., et al. (2008). Spatial mapping of the neurite and soma proteomes reveals a functional Cdc42/Rac regulatory network. *Proc. Natl. Acad. Sci. USA* 105, 1931–1936.
- Ridley, A.J. (2006). Rho GTPases and actin dynamics in membrane protrusions and vesicle trafficking. *Trends Cell Biol.* 16, 522–529.
- Riedl, J., Crevenna, A.H., Kessenbrock, K., Yu, J.H., Neukirchen, D., Bista, M., Bradke, F., Jenne, D., Holak, T.A., Werb, Z., et al. (2008). Lifeact: a versatile marker to visualize F-actin. *Nat. Methods* 5, 605–607.
- Scarpa, E., Szabó, A., Bibonne, A., Theveneau, E., Parsons, M., and Mayor, R. (2015). Cadherin Switch during EMT in Neural Crest Cells Leads to Contact Inhibition of Locomotion via Repolarization of Forces. *Dev. Cell* 34, 421–434.
- Sugiyama, N., Gucciardo, E., Tatti, O., Varjosalo, M., Hyttinen, M., Gstaiger, M., and Lehti, K. (2013). EphA2 cleavage by MT1-MMP triggers single cancer cell invasion via homotypic cell repulsion. *J. Cell Biol.* 201, 467–484.
- Takai, Y., Miyoshi, J., Ikeda, W., and Ogita, H. (2008). Nectins and nectin-like molecules: roles in contact inhibition of cell movement and proliferation. *Nat. Rev. Mol. Cell Biol.* 9, 603–615.
- Theveneau, E., Marchant, L., Kuriyama, S., Gull, M., Moepps, B., Parsons, M., and Mayor, R. (2010). Collective chemotaxis requires contact-dependent cell polarity. *Dev. Cell* 19, 39–53.
- Wong, K., Ren, X.R., Huang, Y.Z., Xie, Y., Liu, G., Saito, H., Tang, H., Wen, L., Brady-Kalnay, S.M., Mei, L., et al. (2001). Signal transduction in neuronal migration: roles of GTPase activating proteins and the small GTPase Cdc42 in the Slit-Robo pathway. *Cell* 107, 209–221.
- Ypsilanti, A.R., Zagar, Y., and Chédotal, A. (2010). Moving away from the midline: new developments for Slit and Robo. *Development* 137, 1939–1952.
- Zaidel-Bar, R., Joyce, M.J., Lynch, A.M., Witte, K., Audhya, A., and Hardin, J. (2010). The F-BAR domain of SRGP-1 facilitates cell-cell adhesion during *C. elegans* morphogenesis. *J. Cell Biol.* 191, 761–769.

Developmental Cell

Supplemental Information

**SrGAP2-Dependent Integration of Membrane Geometry
and Slit-Robo Repulsive Cues Regulates
Fibroblast Contact Inhibition of Locomotion**

**Rafael Dominik Fritz, Denis Menshykau, Katrin Martin, Andreas Reimann, Valeria
Pontelli, and Olivier Pertz**

Supplemental Figures and Legends

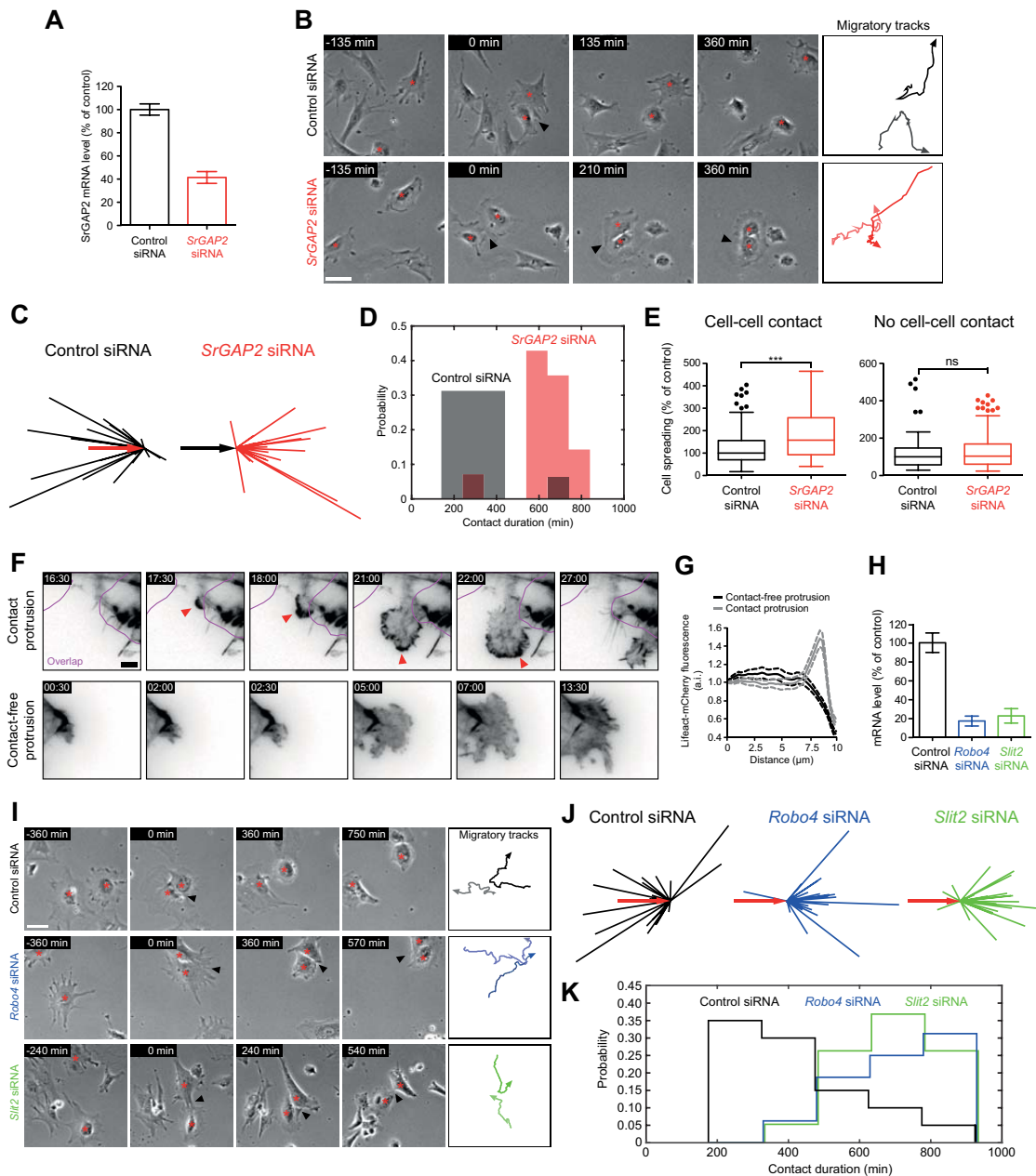


Figure S1. Related to Figures 2, 3, and 5. Slit2-Robo4-srGAP2 signaling regulates CIL in primary MEFs. **(A)** QPCR analysis of srGAP2 KD efficiency. Mean \pm SD of $n = 2$ measurements. **(B)** Phase contrast time series of cell collision between control and srGAP2 KD cells treated with siRNA pools. Migration trajectories are summarized to the right. Black arrowheads designate cell-cell contacts. Time scale, minutes. **(C)** Scaled cell-displacement vectors of colliding cells as described in Figure 2E. $n = 21$ control and 20 srGAP2 KD cells. **(D)** Distribution of cell-cell contact duration in control and srGAP2 KD cells. $n = 16$ and 15 collisions of control and srGAP2 KD cells, respectively. **(E)** Quantification of cell spreading in monolayers (left panel) and subconfluent cells (right panel) transfected with siRNA pools as indicated. Note that srGAP2 regulates contact-dependent spreading only. $n = 113$ and 166 cells (monolayer), 121 and 174 cells (subconfluent). Mann-Whitney test. *** $p < 0.001$; ns, not significant. Boxplots with median, IQR (box) and 1.5 IQR (whiskers), outliers are represented by dots. **(F)** Time series of contact and contact-free protrusions. TIRF images of Lifeact-mCherry cell are shown in

inverted black-white contrast. Magenta line outlines cell-cell overlap. Time scale, minutes:seconds.

(G) Linescans of normalized F-actin intensity in contact and contact-free protrusions imaged by TIRF. Graph displays Mean \pm SEM for n = 21 protrusions for each condition. **(H)** QPCR analysis of knockdown efficiency of pooled siRNAs. Mean \pm SD of n=2 measurements. **(I)** Phase contrast time series of cell collision between control, *Robo4* and *Slit2* KD cells treated with siRNA pools. Migration trajectories are summarized to the right. Black arrowheads designate cell-cell contacts. Time scale, minutes. **(J)** Scaled cell-displacement vectors of colliding cells as described in Figure 2E. n = 21 control, 21 *Robo4* KD and 22 *Slit2* KD cells. **(K)** Distribution of cell-cell contact duration. n = 20, 21 and 18 collisions of control, *Robo4* and *Slit2* KD cells, respectively.

Scale bars, 50 μ m (B,I) and 5 μ m (F).

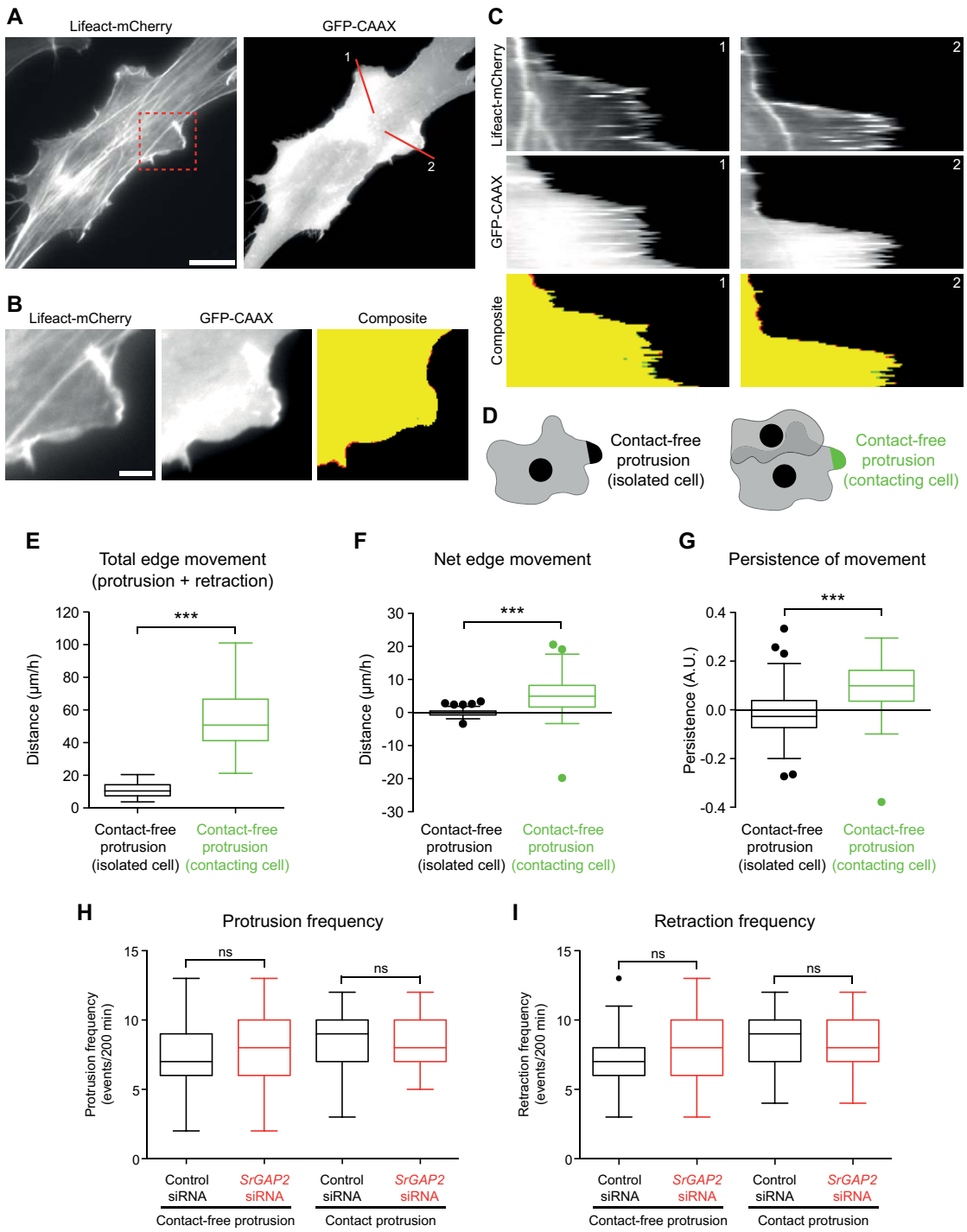


Figure S2. Related to Figures 2 and 3. Additional characterization of protrusion dynamics using the Lifeact reporter. **(A)** Comparison of Lifeact-mCherry and GFP-CAAX as markers of cell dynamics in NIH 3T3 cells. **(B)** Zoom into the red box outlined in (A). Note that both markers overlap perfectly as shown in the overlay of the binary images of each channel. **(C)** Kymograph analysis of cell edge dynamics by Lifeact-mCherry and GFP-CAAX along red lines in (A). Composite images constructed from binary images of each channel show that both markers are well suited to faithfully track edge dynamics. **(D)** Schematics of contact-free protrusions in isolated cells and cells engaged in cell-cell overlap. **(E-G)** Quantification of contact-free protrusion dynamics in isolated cells and cells with cell-cell overlap. The total edge movement (E), net edge movement (F) and persistence of movement (G) are shown. n = 37 and 54 kymographs. Note that the two conditions were obtained from separate

experiments. Two-tailed unpaired Student's t-test (E) and Mann-Whitney test (F, G) were applied. ***
 $p < 0.001$. **(H,I)** Quantification of protrusion frequency (H) and retraction frequency (I) of contact-free
and contact protrusions measured in control and *srGAP2 KD* cells. $n = 87, 64, 54, 39$ kymographs.
Bonferroni's multiple comparison test was used to compare conditions; ns, not significant.
All boxplots with median, IQR (box) and 1.5 IQR (whiskers), outliers are represented by dots. Scale
bars, 20 μ m (A) and 5 μ m (B).

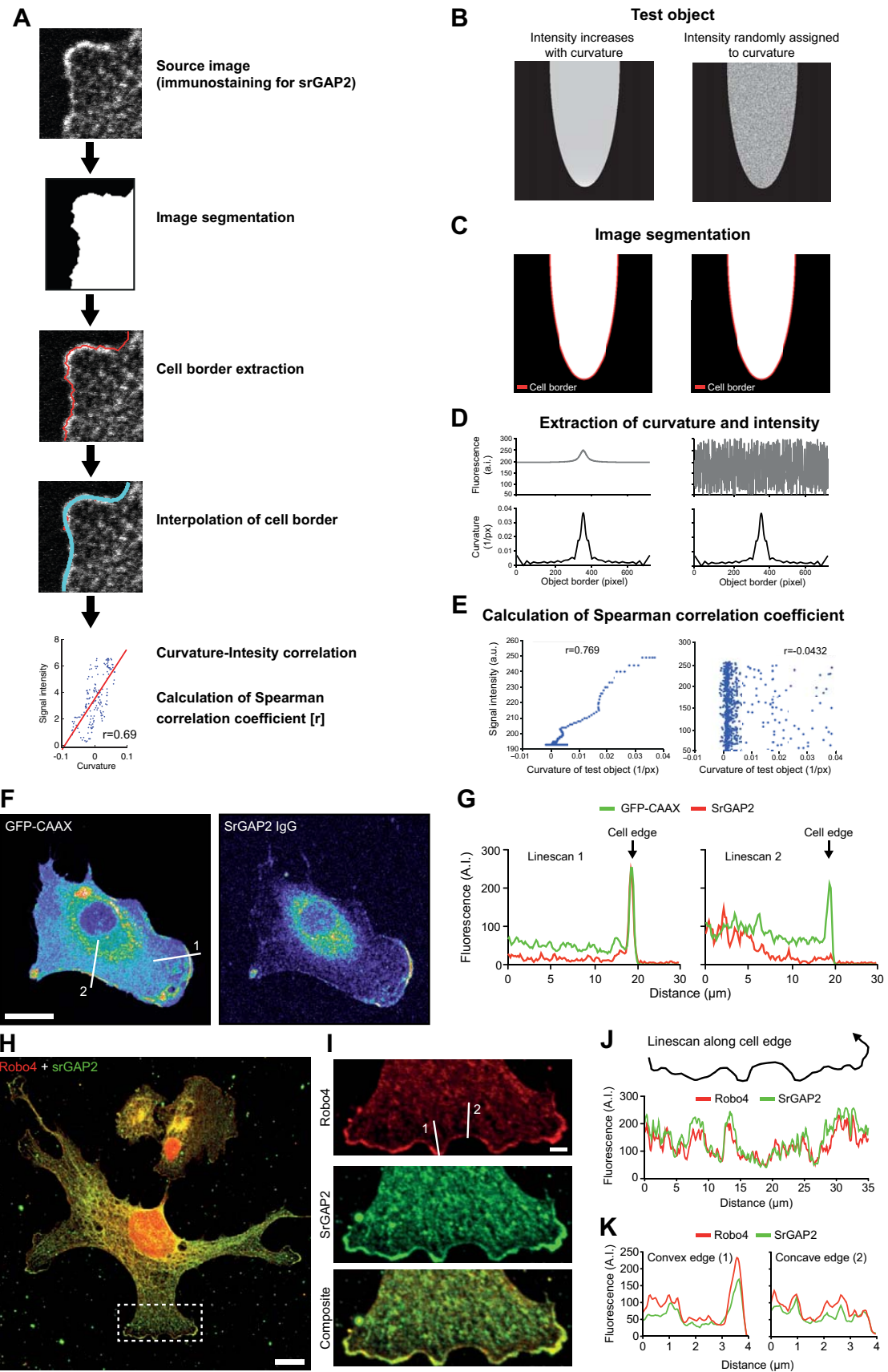


Figure S3. Related to Figure 4. Correlation of srGAP2 signal intensity and cell edge curvature.

(A) Overview of image analysis pipeline. The source image displaying a protrusion immunostained for srGAP2 is segmented so that black and white colors represent background and cell interior,

respectively. The cell border is extracted (red line). The extracted border is then interpolated by 3rd-order polynomial splines yielding the interpolated border (cyan line). Based on the interpolated border, signal intensity and curvature values are extracted along the border and plotted. Spearman correlation coefficient (r) is calculated to test for correlation. SrGAP2 amount at the cell edge positively correlates with cell edge curvature as shown by the high Spearman's correlation coefficient of $r=0.69$. **(B)** To validate the image analysis tool we created synthetic images where signal intensity was a linear function of the curvature (left panel) or a random uniform function (right panel). In the first case, signal intensity rises with increasing curvature and in the second case signal intensity is randomly assigned to curvature. **(C)** Image segmentation. The red line represents the extracted object border. **(D)** Signal intensity (grey line) and object curvature (black line) profiles along the border. Note random fluorescence fluctuations (right panel). **(E)** Correlation of signal intensity and object curvature. Spearman correlation coefficient is shown. Note large positive Spearman correlation coefficient (left panel), where signal intensity raises with increasing curvature. Contrary, in case of random assignment of signal intensity to curvature, the correlation coefficient is close to zero (right panel). These results show that this image pipeline is able to extract signal intensity and curvature profiles along object borders, and to test for correlation of both parameters as measured by the Spearman correlation coefficient. **(F)** Single confocal plane of a cell expressing GFP-CAAX (left panel) and immunostained for endogenous srGAP2 (right panel). The CAAX sequence originates from K-Ras 4b and targets proteins to the plasma membrane (Hancock et al., 1990). **(G)** Linescans along the white lines in (F). Note that srGAP2 signal peaks at curved cell edges and colocalizes with the GFP-CAAX signal (linescan 1). In contrast, no srGAP2 enrichment is detectable at straight cell edges, even despite clear GFP-CAAX concentration (linescan 2). However, the srGAP2 signal, even in the absence of cell edge enrichment, still delineates the cell edge. **(H)** Composite single confocal plane of a cell immunostained for endogenous srGAP2 (green) and endogenous Robo4 (red), which is a plasma membrane protein. **(I)** Zoom into lamellipodium region depicted by dotted box in (H). Note strong enrichment of both srGAP2 and Robo4 at the cell edge. **(J)** Quantification of srGAP2 and Robo4 staining intensity along the edge as outlined in the top panel. **(K)** Linescans through convex and concave regions in the lamellipodium. Note that srGAP2 and Robo4 signals are enriched and colocalize at convex regions of the plasma membrane.

Scale bars, 20 μ m (A), 10 μ m (H) and 2 μ m (I).

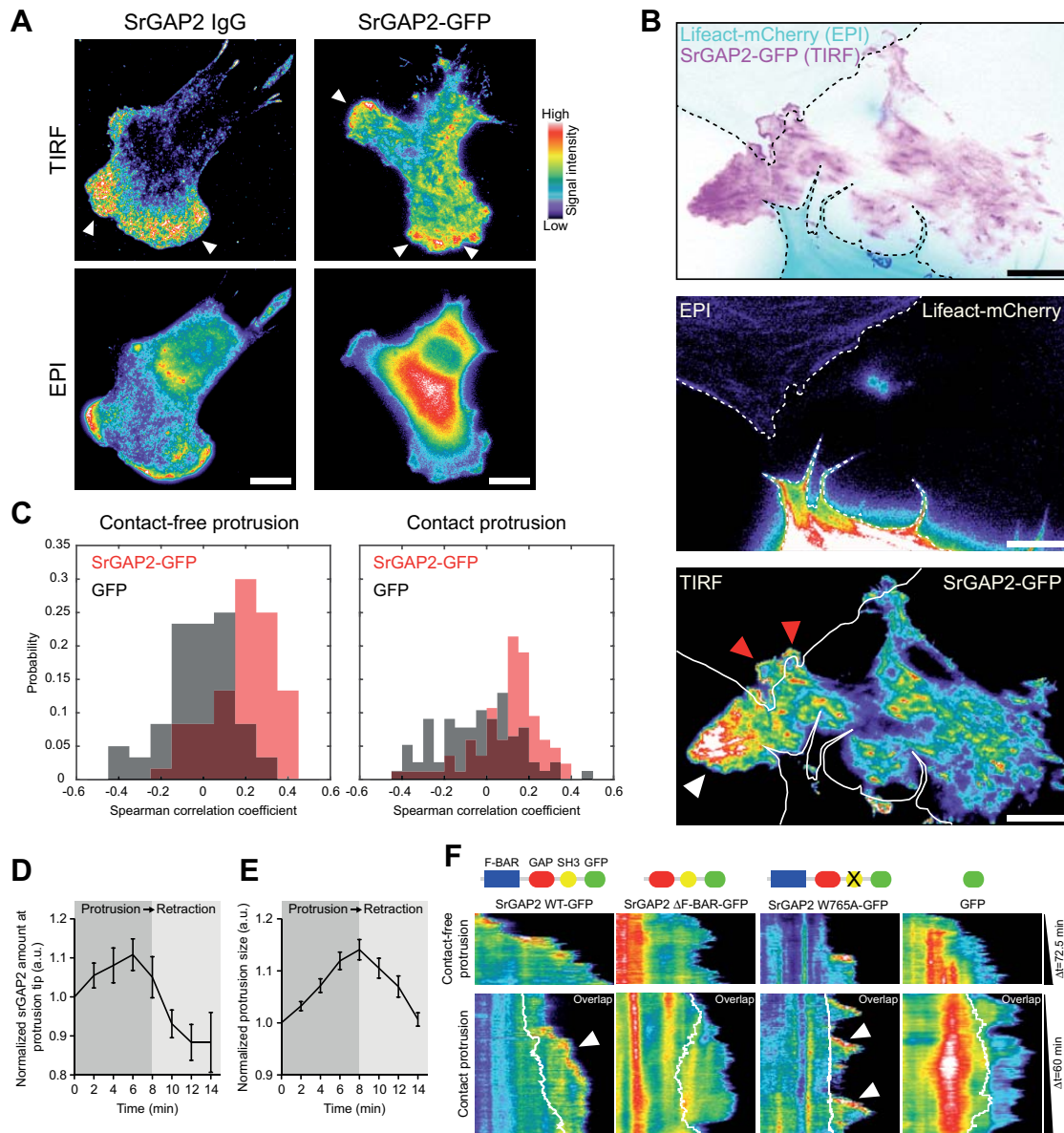


Figure S4. Related to Figure 4. Additional characterization of srGAP2 localization and dynamics in contact-free and contact protrusions.

(A) Comparison of srGAP2 subcellular distribution patterns in polarized cells immunostained for endogenous srGAP2 or transfected with srGAP2-GFP. TIRF and epifluorescence channels are pseudocoloured for signal intensity. White arrowheads indicate srGAP2 accumulation at the leading edge. Both experimental techniques yield similar distribution patterns. Note that broad srGAP2 enrichment is detectable in the TIRF but not the epifluorescence channel. **(B)** Comparison of srGAP2 localization in contact-free and contact protrusions in one cell. Data corresponds to Figure 4I. Lifeact-mCherry and srGAP2-GFP cells are shown in cyan/magenta and pseudocolours. Lines denote cell borders. The upper Lifeact-mCherry cell becomes well detectable in the pseudocoloured epifluorescence image. Note that srGAP2-GFP forms a wide gradient in contact-free protrusions (white arrowhead) but enriches just at the tip of contact protrusions (red arrowheads). **(C)** Distribution of Spearman correlation coefficients for srGAP2-GFP expressing cells (red bars) or GFP expressing cells (grey bars). Cell protrusions were recorded by time-lapse microscopy and $n > 200$ Spearman correlation coefficients between signal intensity and cell edge curvature were computed for each condition and plotted. **(D,E)** Quantification of srGAP2 amount at the tip of contact protrusions (D) and contact protrusion size (E). Graphs represent Mean \pm SEM of $n = 13$

protrusion/retraction events from 13 cells. SrGAP2 activity was quantified based on kymographs within a 4-pixel region at the tip of contact protrusions. **(F)** Kymograph analysis of the dynamics of the exogenously expressed srGAP2 mutants. White lines depict cell-cell overlap regions and white arrowheads point to the focused localization of srGAP2 at the cell edge.

All scale bars, 10 μ m.

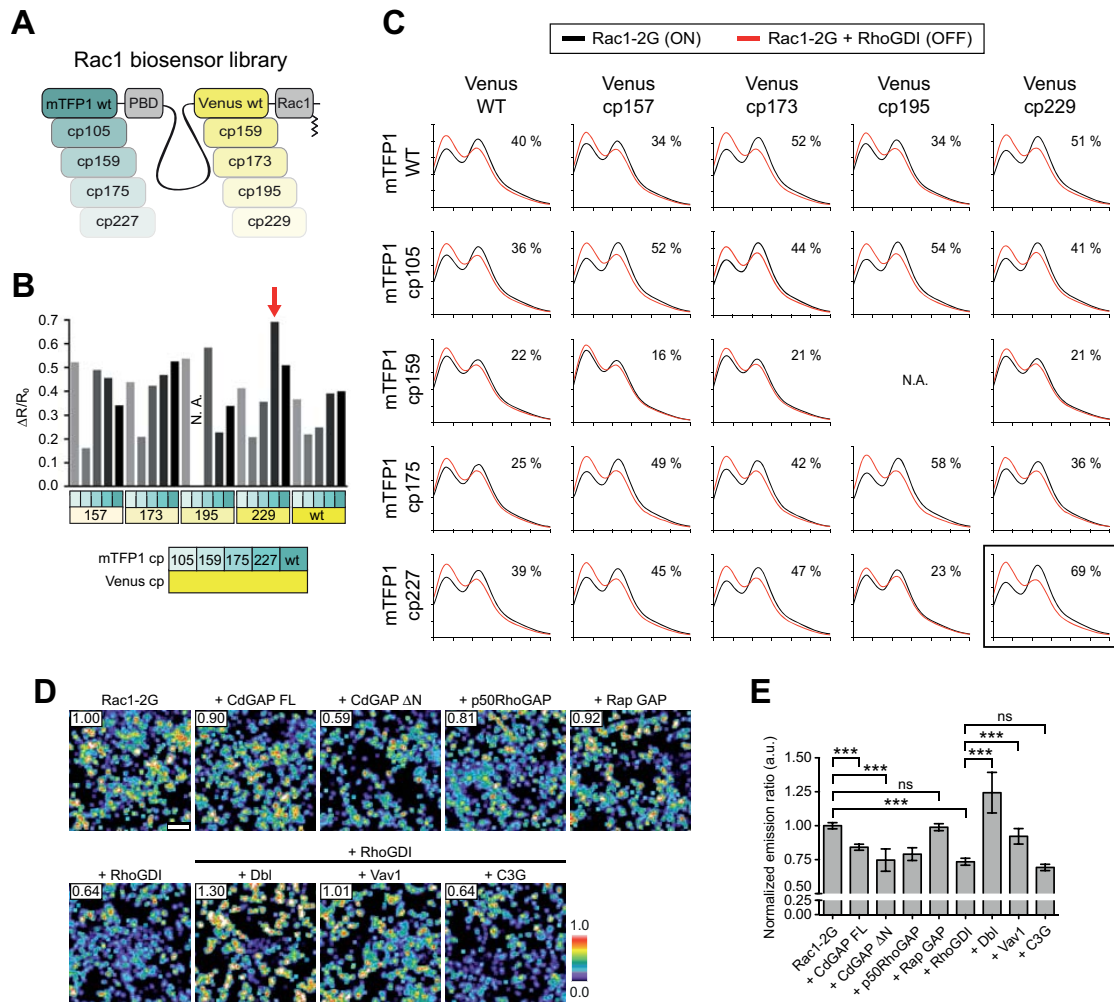


Figure S5. Related to Figure 6. Additional evaluation of the Rac1 biosensor library and the Rac1-2G biosensor.

(A) Schematics of the Rac1 biosensor library. The biosensor contains the FRET donor mTFP1, amino-acids 68-150 of the effector domain of PAK1, an 64 amino-acid linker, the FRET donor Venus, and Rac1. Note that the Rac1 C-terminus remains free for adequate prenylation and reversible interactions with RhoGDI. The library consists of 25 biosensors in which the wild-type or 4 different circularly permuted mutants are used for the donor and acceptor fluorophores. **(B, C)** Evaluation of the dynamic range of the Rac1 biosensor library using fluorometry. Each biosensor was expressed either alone (ON state) or co-expressed with RhoGDI (OFF state) in HEK293FT cells, and emission profiles were measured in cell suspensions using a cuvette-based fluorometer. **(B)** $\Delta R/R_0$ values represent changes in FRET efficiency between the ON and OFF states. A key indicates the specific mTFP1 and Venus mutants. An arrow indicates the selected biosensor. $n = 1$ measurement. **(C)** Normalized emission profiles of the indicated Rac1 biosensors are shown in the ON (black trace) and OFF (red trace) states. $\Delta R/R_0$ values of the indicated biosensors are also shown. Black box indicates the selected biosensor. $n = 1$ measurement. **(D, E)** Evaluation of the Rac1-2G biosensor's response to different upstream regulators using microscopy. Transiently transfected HEK293FT cells were imaged in 96-well plates using high throughput microscopy. Average ER of multiple cells is calculated on a per-field of view basis. **(D)** Representative ratio images of cells co-expressing Rac1-2G and different upstream regulators. Images are color-coded for Rac1-2G activity according to scale. Average, normalized ER is indicated for each condition in the upper left corner. **(E)** Average, normalized ER of Rac1-2G. Bars represent Mean \pm SEM $n = 27$ fields of view containing ≥ 100 cells each. Note similar trends as observed in the corresponding fluorometry experiment in Figure 6D. Scale bar, 50 μ m.

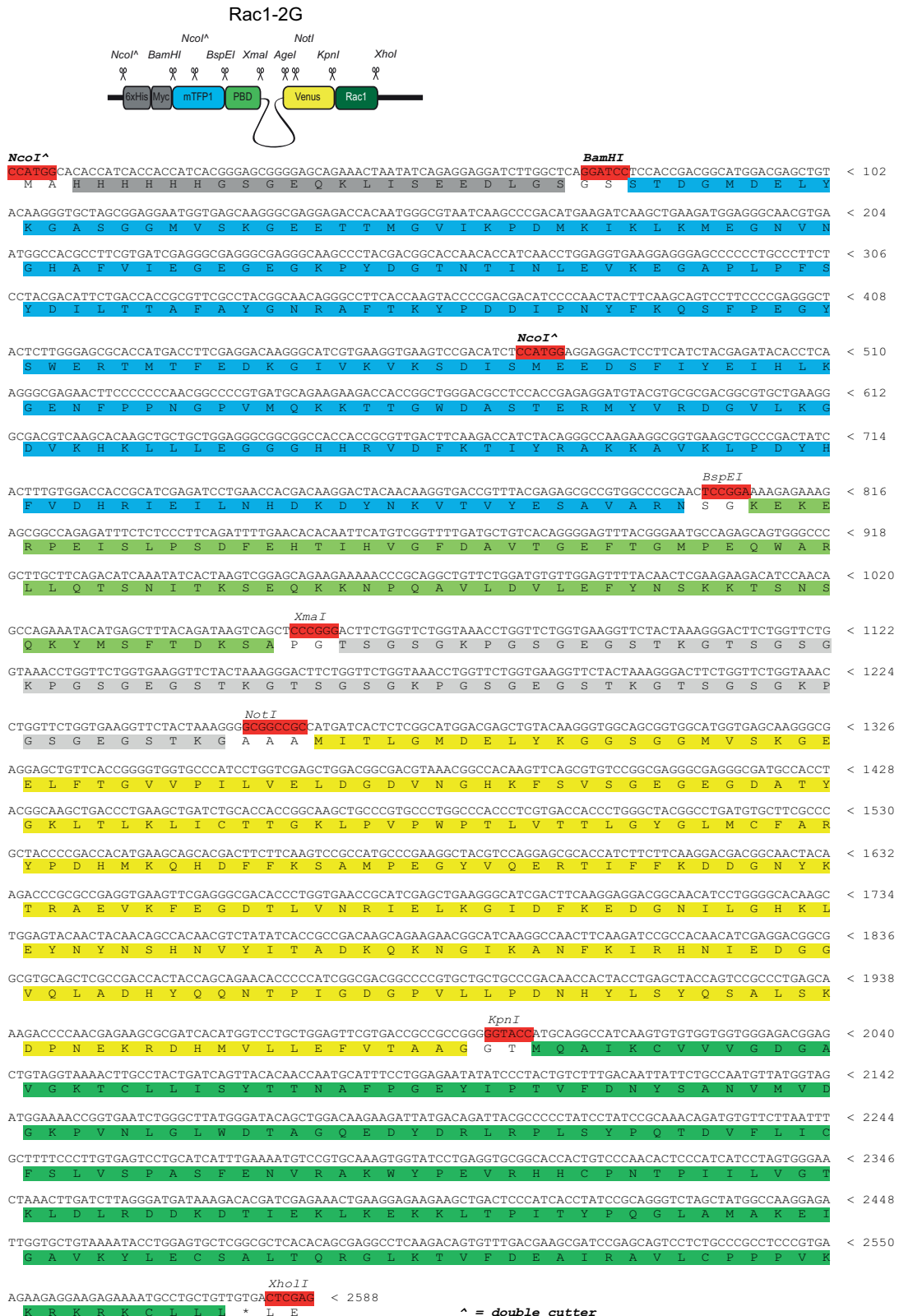


Figure S6. Related to Figure 6. Sequence of Rac1-2G (mTFP1/cp227-Venus/cp229) biosensor.

Different biosensor domains are color-coded according to the scheme displayed above the sequence.
 Different expression plasmids are available at Addgene. Plasmid ID: 66110 (pTriEx-Rac1-2G), 66111 (pLenti-Rac1-2G), 66112 (pAd/CMV/V5-DEST-Rac1-2G).

Supplemental Movie Legends

Movie S1. Related to Figure 2. *SrGAP2* KD cells exhibit deficiency in CIL. Control and *srGAP2* KD fibroblasts were monitored during cell collision by time-lapse microscopy. SiRNA-transfected NIH 3T3 cells and shRNA-treated primary MEFs are shown in top and bottom panels, respectively. Note lack of cell repolarization and change of migration direction in *srGAP2* KD cells after cell-cell collision. Time scale, hours:minutes; 10 (top panels) and 15 (bottom) minute frame rate. Scale bar, 40 μ m.

Movie S2. Related to Figure 2. *SrGAP2* KD cells display increased cell-cell overlap. Control and *srGAP2* KD NIH 3T3 fibroblasts expressing either Lifeact-GFP (magenta) or Lifeact-mCherry (cyan) were monitored during cell collision. Epifluorescence channels (top) and binary masks (bottom) are shown. Control cells show intact repolarization that is lost in *srGAP2* KD cells, which also show increased cell-cell overlap. Time scale, hours:minutes; 5 minute frame rate. Scale bar, 30 μ m.

Movie S3. Related to Figure 3. Cell-cell overlap regions are highly dynamic zones that are constantly explored by contact protrusions. Subconfluently seeded NIH 3T3 wild type fibroblasts expressing Lifeact-GFP (magenta) or Lifeact-mCherry (cyan) were monitored during cell-cell interactions. Epifluorescence and TIRF channels are shown. Note highly dynamic protrusion/retraction cycles in cell-cell overlaps. Zoom is centered on highly dynamic contact protrusions. Comparison of epifluorescence and TIRF channels shows that contact protrusions remain connected with the ECM while moving beneath a quiescent edge of contacting cells. Time scale, minutes:seconds; 30 second frame rate. Scale bar, 20 μ m.

Movie S4. Related to Figure 3. Comparison of contact and contact-free protrusion dynamics. Zoom on contact (left) and contact-free (right) protrusions in the Lifeact-mCherry cell shown in Movie S3. TIRF channel is shown in inverted black-white contrast. Alternating black/white line depicts the border of Lifeact-GFP cell to visualize cell-cell overlap. Note highly focused F-actin band at the tip of contact protrusions. Time scale, minutes:seconds; 30 second frame rate. Scale bar, 2 μ m.

Movie S5. Related to Figure 4. *SrGAP2* dynamics in contact-free and contact protrusions. Adjacent NIH 3T3 cells expressing either Lifeact-mCherry or *srGAP2*-GFP were time-lapsed using epifluorescence and TIRF microscopy. *SrGAP2*-GFP TIRF signal is color-coded for intensity so that warm and cold colors represent high and low *srGAP2* amounts respectively. White lines depict the border of Lifeact-mCherry cells to visualize cell-cell overlap. Note broad and narrow *srGAP2* accumulation in contact-free and contact protrusions, respectively. Red arrowheads point towards focused *srGAP2* enrichment in contact protrusions. Time scale, minutes:seconds; 30 second frame rate. Scale bar, 5 μ m.

Movie S6. Related to Figure 6. Rac1 activation dynamics in REF52 cells stimulated with 40 ng/mL PDGF. Fibroblasts expressing the Rac1-2G FRET biosensor were analyzed by epifluorescence microscopy. Rac1 activation (ratio, left) and biosensor distribution (FRET, right) are color-coded for signal intensity so that warm and cold colors represent high and

low Rac1 activity/amount, respectively. Note broad Rac1 activation gradient in free protrusion that switches off during retraction. Time scale, minutes:seconds; 30 second frame rate. Scale bar, 20 μ m.

Movie S7. Related to Figure 7. Rac1 activation dynamics in contact-free protrusions. NIH 3T3 cells expressing the Rac1-2G FRET biosensor were analyzed by epifluorescence microscopy. Rac1 activation (ratio, left) and biosensor distribution (mTFP1, right) are color-coded for signal intensity so that warm and cold colors represent high and low Rac1 activity/amount, respectively. Note broad Rac1 activation gradient in the contact-free protrusion. Time scale, hours:minutes; 2 minute frame rate. Scale bar, 5 μ m.

Movie S8. Related to Figure 7. Rac1 activation dynamics in contact protrusions. NIH 3T3 cells expressing either the Rac1-2G biosensor or Lifeact-mCherry were seeded and allowed to interact. Fibroblasts expressing the Rac1-2G FRET biosensor were analyzed by epifluorescence microscopy. Rac1 activation (ratio, left) and biosensor distribution (mTFP1, right) are color-coded for signal intensity so that warm and cold colors represent high and low Rac1 activity/amount, respectively. White (left) and black (right) line depicts the border of Lifeact-mCherry cell to visualize cell-cell overlap. Note focused Rac1 activation at the tip of contact protrusions (white arrowheads). Video is repeated once for enhanced visual perception. Time scale, hours:minutes; 2 minute frame rate. Scale bar, 5 μ m.

Supplemental Experimental Procedures

Cell lines and reagents.

NIH 3T3 fibroblasts (ATCC), primary mouse embryonic fibroblasts (kind gift from R. Zeller), rat embryonic fibroblasts (REF52; a kind gift from A. Howe) and human embryonic kidney (HEK) 293 FT cells (Invitrogen) were maintained in Dulbecco's modified eagle medium (DMEM; Sigma) supplemented with 10% fetal bovine serum (FBS; Sigma), 4 mM L-Glutamine (Sigma) and 100 U/ml penicillin/streptomycin (Sigma) at 37°C and 5% CO₂. The following reagents were used in this study: anti-srGAP2 (C-14) and anti-Slit2 (G-19) antibodies were from Santa Cruz, anti-Robo4 (ab10547) antibody was from Abcam and anti-alphaTubulin (DM 1A) antibody from Sigma. Human fibronectin was from Chemicon. PDGF was from Sigma.

Plasmids.

SrGAP2-GFP wild type, ΔF-BAR and W765A mutants were kind gifts from F. Polleux and described earlier (Guerrier et al., 2009). Lifeact-GFP was described recently (Martin et al., 2014). Lifeact-mCherry was generated by fusing the Lifeact coding sequence (Riedl et al., 2008) to the N-terminus of mCherry followed by shuttling of the Lifeact-mCherry fragment into the lentiviral backbone pRRpRRL- SV40(puro)_CMV(mcs) (a kind gift from M. Kaeser) by homologous recombination (InFusion® technology, Clontech). For simultaneous expression of Lifeact-GFP and NLS-mCherry, a bicistronic construct consisting of Lifeact-GFP, the IRES sequence derived from the pIRES vector (Clontech) and NLS-mCherry was assembled in pcDNA3.1 vector and shuttled into pRRpRRL- SV40(puro)_CMV(mcs) using InFusion® technology (Clontech). The following expression constructs were kind gifts from N. Lamarche-Vane (CdGAP), X. Bustelo (Vav1), J. de Rooij (Rap Gap, C3G), G. Bokoch (p50RhoGAP, Dbl), and M. Schwartz (RhoGDI).

Rac1 biosensor construction.

The Rac1 FRET biosensor was constructed using the cpFRET toolkit (Fritz et al., 2013). Following the design yielding the most sensitive 2nd generation RhoA sensor, we constructed 25 sensor variants consisting of mTFP1 wt and four circular permutations (cps), the PAK1 effector domain (amino acids 68-150; custom gene synthesis; GenScript), a 64 amino acid linker, Venus wt and four cps and Rac1 (custom gene synthesis; GenScript). The design including restriction sites used for cloning as well as the sequence of the 2nd generation Rac1 (Rac1-2G) sensor is shown in Figure S6. Importantly, this biosensor architecture allows for lipid modification of Rac1 and therefore preserves the regulation by RhoGDI required to faithfully report on endogenous GTPase activation in time and space as observed elsewhere (Fritz et al., 2013). The most sensitive Rac1-2G sensor containing mTFP1/cp227 and Venus/cp229 was shuttled from pTriEx into the pAd/CMV/V5-DEST Gateway® Vector according to the manufacturers instructions (Invitrogen). The dominant negative (T17N) and effector (Y40C) mutations were generated by site-directed mutagenesis (Stratagene).

Gene downregulation by siRNAs and shRNAs.

An siRNA pool consisting of four individual SMARTPOOL siRNAs (Dharmacon) was used to knock down srGAP2 in most of the experiments unless otherwise stated. The screen for

genes modifying contact-dependent cell spreading was performed with pools consisting of three individual Stealth RNAi siRNAs (Invitrogen) and positive hits were validated with three single siRNA sequences to exclude off-target effects. MISSION shRNA (Sigma) was used for stable knockdown of *srGAP2*. SiRNAs were transfected into NIH 3T3 and primary MEFs cells using DharmaFECT1 (Dharmacon) according to manufacturer's procedures. Knockout efficiency was measured 48h or 72h post transfection by qPCR or Western blot.

The following siRNAs and shRNAs were used:

Stealth RNAi siRNAs (Invitrogen)		
Gene	Order number	5'-3' Sequence
Srgap1_1	MSS202046	GAUCAUAGCCGAGUAUGAAAGUCAA
Srgap1_2	MSS202047	GACUGACCGC CAUUCUGUAAGCUAU
Srgap1_3	MSS202048	ACCAACGCCUCCGGUUUCAAGUAUU
Srgap2_1	MSS204395	ACAUGAAGGU CUGGGAUGCUAUU GAA
Srgap2_2	MSS204396	UCACAAUGUAAGUGAACCGACAUAA
Srgap2_3	MSS274401	GAAGCACCAAGGACCAGCAAUUAAA
Srgap3_1	MSS281821	CCGUGAACUGUU UGGUAUCUGGUACU
Srgap3_2	MSS281822	CACGAUGUCUCUGAU CUCAUCCGAU
Srgap3_3	MSS281823	GAGAGCCAACCAGCAGGAAACAGAA
Robo1_1	MSS208673	CAGCCAU GGUGA AUCCGGAGGGUUA
Robo1_2	MSS208674	GGUGGACCAACAAUCUCAAUAAA
Robo1_3	MSS208675	CAACGCCAUCGGCUGGAGGUAGCUAU
Robo2_1	MSS241004	CCACAUUUCUCAGGAGGCAAUUAAA
Robo2_2	MSS241005	CCCUCAGACUCACUGU CUUUJGAA
Robo2_3	MSS282032	AGGCCA ACACAAUCUACUUGUUUA
Robo3_1	MSS276804	CCACAU GGAAUAGCUGGUUAGGGAA
Robo3_2	MSS276805	CCUGAUCCAGAUGAUAGAUACUACA
Robo3_3	MSS276806	CAAGCCUGUACAAAUGGCAU CUUUG
Robo4_1	MSS232364	CCAGCCAAAGAUGAGGUGGCAGAUCAU
Robo4_2	MSS232365	GCCAU AAUGGUGUCAUCCGGUGGUUA
Robo4_3	MSS232366	GGUCUCAU GGUGGAAAGACGGGAAA
Slit1_1	MSS209183	CCAGGUGUGAGUGCAUGCUAGGUUA
Slit1_2	MSS209184	CCAGGGCCAU GUGCCGGGUUAGGUU
Slit1_3	MSS209185	CCGCCUGGAGUUGAACGGUAUCAAA
Slit2_1	MSS209186	CAUCACACUUCAGAUU GGCCACAGAU
Slit2_2	MSS209187	CCGACUGGGUGAAGUGCAGAAUAAA
Slit2_3	MSS209188	CCCGUCUGGGUGUAGGAAAUUCUU
Slit3_1	MSS209189	ACUGUGACUGCAGUCUGCGUUGGUU
Slit3_2	MSS209190	UGGUGAUGCUAA ACCAGACCCUGAA
Slit3_3	MSS209191	GGCUCUGAGGAUUAUCGCAACAGAU
Negative Control medium GC Duplex	12935-300	
siGENOME SMARTPOOL siRNAs (Dharmacon)		
Gene	Order number	5'-3' Sequence
SrGAP2_1	D-040298-01	GAGGAAGCAUGGAGGAUUA
SrGAP2_2	D-040298-02	GUAGGAACCUCAUCACAAA
SrGAP2_3	D-040298-03	GCAAAUCAGUAAAGCAAGA
SrGAP2_4	D-040298-04	UUUCCUAUCUGCUGAAUUA
siGENOME Non-Targeting siRNA Pool #1	D-001206-13-05	
MISSION shRNA (Sigma)		
Gene	TRC number/Order number	5'-3' Hairpin sequence
SrGAP2	TRCN0000271904	CCGG-CATGACCTGTCTGATATTATT-CTGAG-AATAATATCAGACAGGTATG-TTTTG
Non-targeting Control	SHC002	

Lentiviral-mediated generation of stable cell lines.

Lentiviral particles were produced as described before (Fritz et al., 2013). Briefly, 3x10⁶ HEK293FT cells were seeded on Poly-L-Lysine (PLL; 10 µg/mL; Sigma) in 10cm dishes and transfected 24h later with pRRpRRL-SV40(puro)_CMV(mcs) containing the gene of interest or pLKO-shRNA together with pVSV, pMDL and pREV packaging plasmids using Fugene HD. Culture supernatants were collected 72h and 96h post transfection, filtered through 0.45µm filters (Sarstedt) and concentrated with Lenti-X reagent (Clontech) at 4°C according to manufacturer's procedures. Virus particles were harvested by centrifugation at 1500xg for 45 minutes at 4°C and resuspended in DMEM supplemented with 10% FBS, 4 mM L-Glutamine and 100 U/ml penicillin/streptomycin. 2x10⁴ NIH 3T3 cells seed 24h before into

12-well plates were then infected with different virus dilutions (1:2 to 1:40 range) in the presence of 5 μ g/mL Polybrene (Sigma). Cells with unaffected morphology and low but sufficient expression of the gene of interest were selected with 5 μ g/mL puromycin (Sigma).

Adenoviral infection.

The Rac1 FRET biosensor was expressed in NIH 3T3 and REF52 cells by adenoviral gene delivery. Viral particles were generated using the pAd/CMV/V5-DEST Gateway® Vector system (Invitrogen) following manufacturer's instructions. For infection, 3x10⁴ NIH 3T3 cells were seeded into 12-well plate and grown in DMEM supplemented with 10% FBS, 4 mM L-Glutamine and 100 U/ml penicillin/streptomycin for 6h. Following overnight incubation with adenoviral particles, cells were rinsed with PBS, reseeded and imaged 40h post infection.

Immunofluorescence.

1-2x10⁴ NIH 3T3 cells were seeded on 18mm or 24mm glass cover slips coated with 5 μ g/mL fibronectin and cultured overnight in DMEM supplemented with 10% FBS, 4 mM L-Glutamine and 100 U/ml penicillin/streptomycin at 37°C. Cells were rinsed once in PBS, fixed in 4% paraformaldehyde for ten minutes at room temperature and permeabilized with 0.1% Triton-X 100 for two minutes. Subsequently, cells were blocked for ten minutes in 2% BSA and incubated with the following primary antibodies for 60 minutes at room temperature: anti-srGAP2 (C-14; 1:100), anti-Slit2 (G-19; 1:50) and anti-Robo4 (1:100). Cells were rinsed three times in PBS before incubation with donkey anti-goat IgG Alexa488 and donkey anti-rabbit IgG Alexa546 (both Invitrogen; 1:1000) for 60 minutes. Cells were rinsed three times in PBS and mounted in ProLong Gold (Invitrogen) for confocal microscopy. For TIRF and epifluorescence microscopy, coverslips were mounted into life cell imaging chambers (Life Cell Instrument) and cells imaged in PBS.

Quantification of cell edge dynamics, protrusion size and F-actin content.

Cell edge dynamics were extracted from kymographs generated with MetaMorph (Molecular Device) based on time-lapse data of contact and contact-free protrusions. Kymographs were segmented and analyzed using MATLAB to quantify individual protrusion and retraction events. From these two parameters, total edge movement, net edge movement and protrusion/retraction frequencies were derived.

To measure normalized protrusion size in time, ratio images were thresholded according to intensity and a region was created around a contact protrusion. Protrusion size was measured in pixels in each frame of the time-lapse movie. Protrusion size was then normalized to the first measured frame of the time-lapse movie.

F-actin was measured along a line placed within contact and free protrusions. The signal from the TIRF channel was quantified in MetaMorph (Molecular Devices).

Supplemental References

Fritz, R.D., Letzelter, M., Reimann, A., Martin, K., Fusco, L., Ritsma, L., Ponsioen, B., Fluri, E., Schulte-Merker, S., van Rheenen, J., *et al.* (2013). A versatile toolkit to produce sensitive FRET biosensors to visualize signaling in time and space. *Sci Signal* 6, rs12.

Guerrier, S., Coutinho-Budd, J., Sassa, T., Gresset, A., Jordan, N.V., Chen, K., Jin, W.L., Frost, A., and Polleux, F. (2009). The F-BAR domain of srGAP2 induces membrane protrusions required for neuronal migration and morphogenesis. *Cell* 138, 990-1004.

Hancock, J.F., Paterson, H., and Marshall, C.J. (1990). A polybasic domain or palmitoylation is required in addition to the CAAX motif to localize p21ras to the plasma membrane. *Cell* 63, 133-139.

Martin, K., Vilela, M., Jeon, N.L., Danuser, G., and Pertz, O. (2014). A growth factor-induced, spatially organizing cytoskeletal module enables rapid and persistent fibroblast migration. *Dev Cell* 30, 701-716.

Riedl, J., Crevenna, A.H., Kessenbrock, K., Yu, J.H., Neukirchen, D., Bista, M., Bradke, F., Jenne, D., Holak, T.A., Werb, Z., *et al.* (2008). Lifeact: a versatile marker to visualize F-actin. *Nat Methods* 5, 605-607.